Explosion Mechanisms of Core-Collapse Supernovae

Hans-Thomas Janka

Max Planck Institute for Astrophysics, D-85748 Garching, Germany;
email: thj@mpa-garching.mpg.de

Keywords

Abstract

Supernova theory, numerical and analytic, has made remarkable progress
in the past decade. This progress was made possible by more sophisticated
simulation tools, especially for neutrino transport, improved microphysics,
and deeper insights into the role of hydrodynamic instabilities. Violent,
large-scale nonradial mass motions are generic in supernova cores. The
neutrino-heating mechanism, aided by nonradial flows, drives explosions,
albeit low-energy ones, of O-Ne-Mg-core and some Fe-core progenitors.
The characteristics of the neutrino emission from newborn neutron
stars were revised, new features of the gravitational-wave signals were
discovered, our notion of supernova nucleosynthesis was shattered, and our
understanding of pulsar kicks and explosion asymmetries was significantly
improved. But simulations also suggest that neutrino-powered explosions
might not explain the most energetic supernovae and hypernovae, which
seem to demand magnetorotational driving. Now that modeling is being
advanced from two to three dimensions, more realism, new perspectives,
and hopefully answers to long-standing questions are coming into reach.

Contents

1. INTRODUCTION: ROOTS AND QUESTIONS

When, why, and how can the catastrophic infall of the core of a massive star be reversed to trigger the powerful ejection of the stellar mantle and envelope in a supernova (SN) explosion? This fundamental problem of stellar astrophysics has been the subject of intense research since Burbidge et al. (1) identified the crucial role played by SNe in the synthesis of heavy elements and in the dissemination of the nuclear burning products of stars. These authors also noticed that nuclear statistical equilibrium (NSE) in the hot, dense core of evolved stars (at $T \gtrsim 7 \times 10^9$ K) favors iron (Fe) dissociation to α particles, and they concluded that the huge demand of energy (~1.7 MeV per nucleon or 1.7×10^{18} erg per gram) must be supplied by gravitational binding energy, which causes contraction of the stellar core and ultimately a dynamical implosion on a timescale of less than 1 s, $t_{\rm coll} \sim 0.21/\sqrt{\rho_8}$ s, when the average density $[\rho_8 \equiv \rho/(10^8 \text{ g cm}^{-3})]$ exceeds unity. This groundbreaking insight is in line with Baade & Zwicky's (2) earlier idea that SNe could represent the transition of ordinary stars to neutron stars (NSs).

By 1960, Hoyle & Fowler (3) had already proposed the two basic scenarios of stellar death: thermonuclear runaway at degenerate conditions [which, as we now know, drives the destruction of white dwarf (WD) stars in type Ia SNe] and the implosion of stellar cores [associated with what

are known as core-collapse SNe (CCSNe) of types II and Ib/c, and hypernovae (HNe)[1]]. Hoyle & Fowler hypothesized (following Reference 1) that the gravitational compression of the core raises the temperature such that thermonuclear fuel can be ignited to release the energy for triggering the ejection of the outer parts of the star. They also mentioned simulations by Colgate & Johnson (4) and Colgate et al. (5), in which the "bounce" of a forming NS launched a spherical shock wave that reversed the infall of the overlying stellar shells to make them gravitationally unbound. Colgate & White (6) realized that gravitational binding energy of order $E_b \sim GM_{NS}^2/R_{NS} > 10^{53}$ erg, which is released when the core of a star collapses to a NS, is converted to neutrino emission and provides a huge energy reservoir for powering the SN blast wave. These authors correctly argued that in stellar layers pulled inward at supersonic speed along with the imploding core, thermonuclear combustion is unable to initiate an outward acceleration. Instead, they proposed that a fraction of the intense neutrino flux may get absorbed in the mantle of the star to cause the explosion.

More than four decades of theoretical and numerical modeling work, spearheaded by early pioneers of the field such as Dave Arnett, Jim Wilson, Hans Bethe, Gerry Brown, Steve Bruenn, Wolfgang Hillebrandt, Jim Lattimer, and David Schramm, have helped improve our knowledge of the diverse physical ingredients and processes that play a role in the core of dying stars, among them magnetohydrodynamic (MHD) effects, fluid instabilities and turbulent flows, the finite-temperature equation of state (EoS) of NS matter, neutrino transport and neutrino-matter interactions, and general relativistic gravity. Although the bounce-shock mechanism is not supported by any modern simulation with state-of-the-art treatment of the physics, the so-called delayed neutrino-heating mechanism, discussed by Bethe & Wilson (7) and aided by violent, nonradial mass motions in the collapsing stellar core (8–11), has become the most favored mechanism powering the majority of SNe.

The momentum behind the quest to solve the puzzle of the SN mechanism originates from the following important questions at the interface between astrophysics and nuclear, particle, and gravitational physics.

1. What is the link between the properties of SNe and their progenitor stars?
2. Which stars collapse to black holes (BHs) instead of NSs, and which fraction of stellar collapses do not yield explosions?
3. What are the birth properties of the compact remnants, namely their masses, spins, magnetic fields, and recoil velocities?
4. How can the high velocities of young pulsars be explained? Is any exotic physics necessary?
5. What characteristics does the neutrino burst from a SN have, and what does the neutrino burst tell us about neutrino properties and the extreme conditions in the newly formed NS?
6. What is the gravitational-wave (GW) signature of a stellar collapse event, and what information can we extract about the dynamical processes in the SN core?
7. What is the nucleosynthetic role of massive star explosions in the chemogalactic history?
8. Are SNe the long-sought sources of r-process elements, especially of the lanthanides, the third abundance peak, and actinides?

---

[1]Observationally, SNe II exhibit strong H Balmer lines in their early spectra, whereas SNe I spectra show no H lines. In SNe Ia there are silicon (Si) lines; in SNe Ib there are no Si lines but there are He lines; and in SNe Ic there are none of these, which indicates that SNe Ic are explosions of stars that had lost their H envelope or both the outer H and He shells before collapse. More subclasses have been introduced, some of which are motivated only by recent discoveries: SNe II-P and II-L are discriminated by a plateau phase or linear decay of their light curves after the peak; SNe IIb events have only thin H shells left; and spectra of SNe IIa and IIn cases possess signatures of a dense circumstellar medium.

9. What is the population-integrated energetic footprint left by SN explosions in the dynamical evolution of galaxies?

In the following sections, we review the known types of stellar collapse events (Section 2), the components and current status of numerical modeling (Section 3), the mechanisms by which massive stars may explode (Section 4), and the signatures of the explosion mechanism that may serve for observational diagnostics (Sections 5 and 6). We provide an update of recent developments as a follow-up to and supplement of previous reports that have approached the topic from different perspectives (12–19).

2. ROUTES TO STELLAR CORE COLLAPSE

Massive stars possess finite lifetimes of millions to tens of millions of years, which are determined mainly by the period the star spends on the main sequence during central hydrostatic hydrogen (H) burning. The evolution time of stars scales approximately as $t_{\text{evol}} \approx 7.3 \times 10^9$ years $(M_*/M_\odot)/(L_*/L_\odot)$, where M_* is the stellar mass and the luminosity is $L_*/L_\odot \approx (M_*/M_\odot)^{3.5}$ (here, $M_\odot = 1.989 \times 10^{33}$ g and $L_\odot = 3.85 \times 10^{33}$ erg s^{-1} are the solar mass and the luminosity, respectively). When H in the stellar core gets exhausted and the star leaves the main sequence, its evolution speeds up considerably because the efficiency of energy production in the higher stages of nuclear burning decreases, and concurrently energy losses through neutrino-antineutrino pairs rise dramatically. This is especially true when the central temperature of the star climbs to $T_c \sim 10^9$ K, at which time $e^+ e^-$ pairs become abundant and the energy drain in $\nu\bar{\nu}$ pairs accelerates with T_c^9. At that time, neutrino losses exceed the radiation losses of the star, and the evolution of the helium (He) core decouples from that of the stellar envelope.

The energy drain occurs at the expense of gravitational binding, leading to continuous contraction of the stellar core, which is slowed down only temporarily by the periods of nuclear burning. As long as nondegenerate particles dominate the pressure of the stellar plasma, hydrostatic equilibrium requires that the central temperature, T_c, and central density, ρ_c, roughly follow the proportionality

$$\frac{T_c^3}{\rho_c} \propto M_c^2 \sim \text{constant}. \qquad 1.$$

According to this relation, more massive stars with larger He cores (larger M_c) are hotter (**Figure 1**). For a sufficiently high central temperature, nuclear fuel can ignite in the next burning stage, building up heavier and more stable elements in their inner core. If, however, the stellar interior enters the regime of electron degeneracy beforehand[2] (**Figure 1**), then it ends as a WD; it is stabilized by lepton degeneracy pressure and cools at an essentially fixed density.

Stars beyond certain birth-mass limits can reach the "death zones" (**Figure 1**) where the stellar core becomes gravitationally unstable. Contraction, and in the case of a runaway process, ultimately collapse, sets in when the effective adiabatic index drops below the critical value of 4/3 for mechanical stability (the actual value is slightly decreased by rotation and increased by general relativistic gravity). Three different processes can initiate the implosion of stellar cores in three areas of the $\rho_c - T_c$ plane, which play a role in different kinds of core-collapse events.

---

[2]Fermions approach the degeneracy when their Fermi energy begins to exceed the thermal energy $k_B T$, that is, at $T_8 \lesssim 4\rho_5^{2/3}$ for nonrelativistic electrons and at $T_{10} \lesssim \rho_8^{1/3}$ for relativistic ones with $T_x \equiv T/(10^x \text{ K})$ and $\rho_y \equiv \rho/(10^y \text{ g cm}^{-3})$.
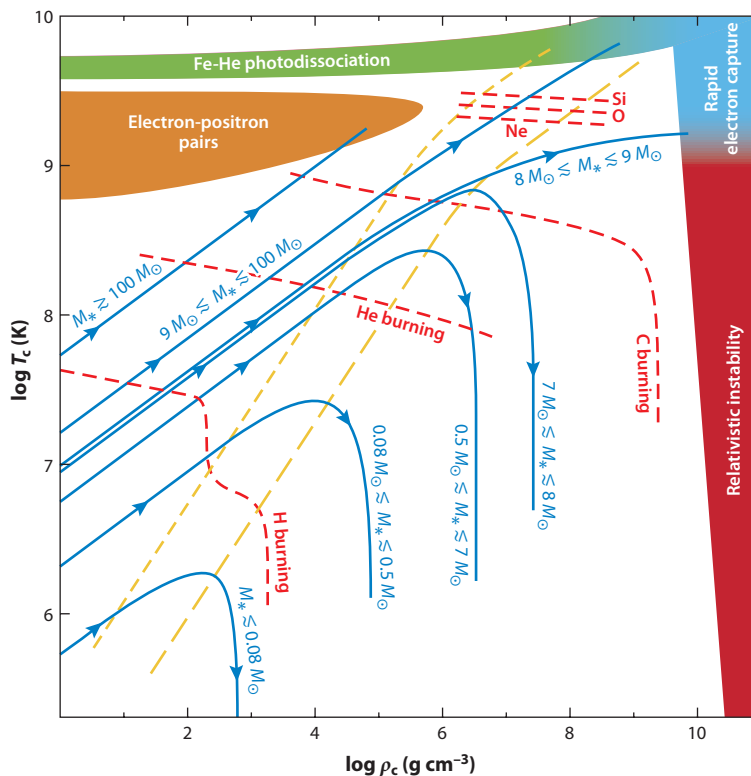
Figure 1

Stellar death regions with schematic stellar evolution tracks in the plane of central density (ρ_c) and central temperature (T_c). Colored death regions are labeled by the instability process causing the collapse of the stellar core, and the blue tracks are labeled by the corresponding rough birth-mass range of objects reaching the different stages of central burning (*red dashed lines*). The yellow diagonal lines mark the beginning of degeneracy (*short-dashed line*) and strong degeneracy (*long-dashed line*) of the electron plasma. Note that realistic stellar tracks exhibit wiggles and loops when the ignition of the next burning stage is reached and the stellar core adjusts to the new energy source (20).

2.1. Electron-Capture Supernovae

The lowest-mass progenitors of CCSNe develop oxygen-neon-magnesium (O-Ne-Mg) cores through carbon (C) burning (21, 28, 29) but reach electron degeneracy before hydrostatic Ne burning can be ignited. Due to the low reaction thresholds of Ne and Mg, the increasing electron Fermi energy enables electron captures (**Figure 1**), triggering gravitational collapse and resulting in an electron-capture SN (ECSN). Solar-metallicity stars[3] with a mass of 9 to 9.25 $M_\odot$ are estimated to have that fate (29), but the mass window is expected to shift and widen for lower metallicities (30) and in binary systems with mass loss or transfer (31), so ECSNe could contribute 20–30% of all SNe (32, 33).

Because of the extremely steep density decline in a thin C-O shell ($\sim$0.1 $M_\odot$ between approximately 3×10^4 g cm^{-3} and 4×10^8 g cm^{-3}) at the edge of the O-Ne core (**Figure 2**), these stars

---

[3]The metallicity Z is the total mass fraction of chemical elements heavier than He in the matter from which the star was formed. The solar value has been determined to be 0.016.
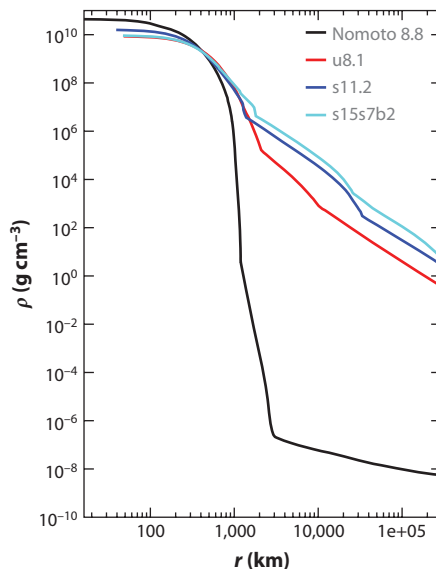
Figure 2

Core-density profiles of different supernova (SN) progenitors at the onset of gravitational collapse. The black line corresponds to the O-Ne-Mg core of an 8.8-$M_\odot$ star (21). The other three are SN progenitors with iron cores: an 8.1-$M_\odot$ ultra-metal-poor (10^{-4} solar-metallicity) star (A. Heger, private communication) and 11.2-$M_\odot$ (22) and 15-$M_\odot$ (23) solar-metallicity stars. The steps and kinks in the curves correspond to composition-shell interfaces (Fe-Si and O-C for the 11.2- and 15-$M_\odot$ models and inner and outer boundaries of a C-O-Ne layer for the 8.1-$M_\odot$ case).

have special explosion properties (Section 4.3). They eject little C and O and very little Ni (nickel); therefore, their SNe are relatively faint. The Crab remnant of SN 1054 is thought to be the relic of such an explosion (34, 35), and an increasing number of dim events such as SNe 1997D, 1999br, 2005cs, and 2008S and other recently observed transient sources are being discovered as possible candidates.

2.2. Iron-Core Supernovae

Massive stars that ignite hydrostatic Ne burning form a Fe core. The latter becomes gravitationally unstable when NSE at temperatures around 10^{10} K ($k_B T \sim 1$ MeV) favors the dissociation of Fe-group nuclei to α particles and a growing number of free nucleons (**Figure 1**). With the onset of contraction and increasing density and electron chemical potential, electron captures on nuclei (and some free protons) speed up and accelerate the implosion. The dynamical collapse is abruptly stopped only when nuclear densities ($\rho \gtrsim 2.7 \times 10^{14}$ g cm^{-3}) are reached, and the phase transition to homogeneous nuclear matter leads to a sudden increase of the effective adiabatic index due to repulsive short-range forces between nucleons.

When the overshooting inner core rebounds and crashes supersonically into the subsequently infalling layers, sound waves steepen into a shock front that ultimately leads to the disruption of the star in the SN explosion. However, unlike the situation in O-Ne-Mg cores, the much flatter density profile in and around Fe cores (**Figure 2**) leads to long-lasting, high mass-accretion rates and large ram pressure of the infalling shells. The higher rates and pressure impede the outward propagation of the shock and make Fe-core progenitors harder to blow up than stars

with O-Ne-Mg cores. Although more massive stars exhibit a gross tendency to larger He cores and shallower density decline, the variation with stellar birth mass is not necessarily monotonic (22). The mechanism(s) by which ECSNe and Fe-core SNe succeed to explode are discussed in Section 4.

Stellar cores of pre-SN stars are expected to rotate relatively slowly, that is, with average precollapse spin periods of tens of seconds or more. This slow rotation is a consequence of angular momentum loss associated with mass-loss phases (in particular, when a given star becomes a red giant) because magnetic torques from fields generated by differential rotation in the star couple core and envelope and thereby transport angular momentum efficiently out of the core (36). Stellar rotation is therefore not expected to play a crucial role in the explosion mechanism of normal CCSNe (Section 4.4).

2.3. Gamma-Ray Burst Supernovae

Rapid stellar rotation, however, is thought to be crucial in the case of γ-ray burst (GRB) SNe and HNe (for a review, see Reference 15). HNe originally obtained their name because of their exceptional brightness and thus high Ni production (37), but they are now considered to be stellar explosions with unusually high ejecta velocities (i.e., very broad spectral lines) and therefore high kinetic energies (**Figure 3**) (38). HNe are associated with long-duration ($t_{GRB} \gtrsim 2$ s) GRBs, observed either spectroscopically (e.g., SN 1998bw with GRB 980425, SN 2003dh with GRB 030329, SN 2003lw with GRB 031203, SN 2006aj with GRB 060218, and SN 2010bh with GRB 100316D) or as late light-curve humps superimposed on the power-law decline of the afterglow that follows the GRB.

GRBs, given their extremely luminous, high-energy radiation, are understood to be ultra-relativistic, collimated outflows (i.e., jets). The line profiles (in particular double-peaked oxygen emission lines) observed in many HNe suggest strong global asymmetry. Such events are interpreted as signatures of BH-forming stellar collapses [collapsars (39)], in which matter around rapidly spinning BHs sets free energy in neutrinos, electromagnetic Poynting flux, and mass outflow with an efficiency of up to roughly 40% of the rest-mass energy of accreted material: $\dot{E}_{acc} \lesssim 0.4 \dot{M} c^2 \sim 10^{54} [\dot{M}/(M_\odot \ s^{-1})]$ erg s^{-1}. Alternatively, a nearly critically rotating NS ($t_{rot} \sim 1$ ms) with an ultrastrong dynamo-generated magnetic field, $\langle B \rangle \gtrsim 10^{15}$ G (i.e., a millisecond magnetar), may be the central engine of GRBs and HNe. The jet and stellar explosion could be powered either by the rotational energy of the magnetar or by the gravitational and rotational energy of the accretion flow and BH. Both can be tapped by magnetic fields through MHD effects (Section 4.4) and by neutrinos radiated from matter heated by magnetically generated viscous dissipation (40). The existence of expected strong disk "winds" with the observed large Ni production (15), however, seems to be challenged by MHD simulations (41).

The progenitors of collapsars and GRBs and HNe are thought to possess massive cores that form BHs instead of exploding beforehand. The progenitors must be compact stars without an extended H envelope to allow jets to emerge ultrarelativistically. In other words, the crossing time of the jet must be shorter than the on time of the central engine: $R_*/c \lesssim t_{engine}$. Moreover, the collapsing stellar core must contain a high specific angular momentum [$j \gtrsim GM_{BH}/c \gtrsim 10^{16} \ M_{BH}/(3 \ M_\odot)$ cm^2 s^{-1}] to either form a magnetar with the necessary huge reservoir of rotational energy or allow for a thick, massive accretion disk that remains around the newly formed BH long enough to efficiently release energy.

Such requirements favor rapidly rotating Wolf–Rayet stars as progenitors, but special initial conditions (a high birth spin) and evolution paths that avoid combined mass and angular momentum loss (or, alternatively, binary scenarios) are necessary (42, 43). In the present-day universe,
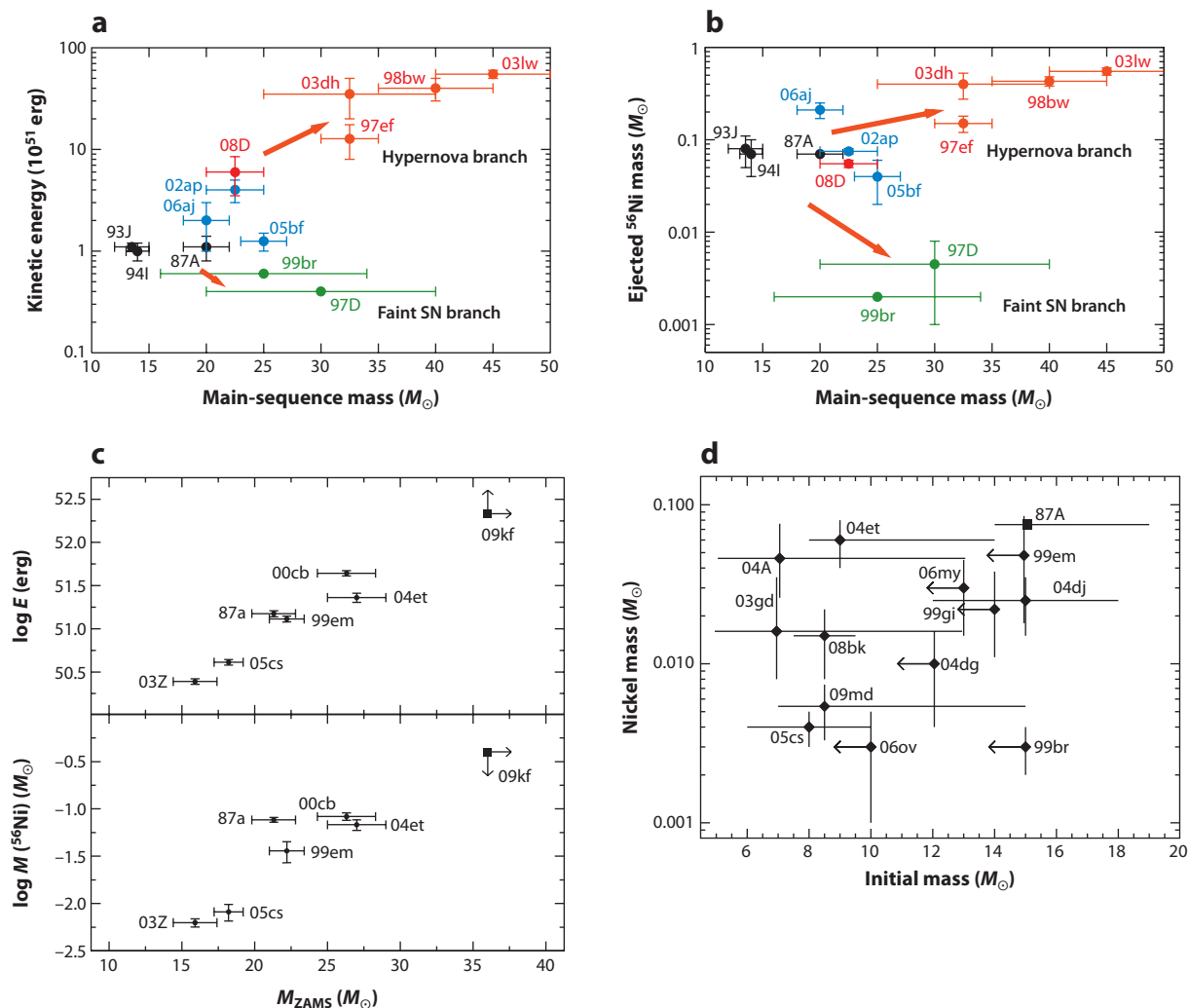
Figure 3

Kinetic energies and ejected nickel masses for stellar explosions versus initial [zero-age main-sequence (ZAMS)] masses reported by different authors. Whereas explosion properties are deduced by comparing observations with light-curve and spectra calculations based on (spherically symmetric) models, the ZAMS masses are estimated by linking ejecta masses to initial masses (*a–c*) through stellar evolution models with mass-loss assumptions (24, 25) or (*d*) by inferring ZAMS masses or upper limits from computed stellar evolution histories that account for the properties of discovered supernova (SN) progenitors or their stellar environments (i.e., coeval star clusters, host galaxies) (26, 27). Due to theoretical uncertainties, both approaches lead to largely different mass determinations for some cases (e.g., SN 1987A, SN 1999br, SN 1999em, SN 2004et, and SN 2005cs). For masses $\gtrsim 25\ M_\odot$, Tanaka et al. (24) discerned a very energetic and bright hypernova branch from a low-energy, faint SN branch. The objects with low nickel production of the latter branch, however, have also been interpreted as weak explosions (possibly electron-capture SNe) near the lower mass limit for SN progenitors. Panels *a* and *b* reproduced with permission from AAS. Panel *c* reproduced with permission from ESO. Panel *d* kindly provided by J. Eldridge and S. Smartt.

HNe and GRB SNe are rare (given a GRB/SN ratio of ~1/1,000, fewer than 1% of all type Ib/c SNe produce GRBs), but BH-forming core-collapse events and GRBs could be very common in the early (solar metallicity ≤1/10) universe. This theoretical expectation is compatible with the fact that GRB SNe are preferentially (but not exclusively) observed in low-metallicity environments.

2.4. Pair-Instability Supernovae

Stars whose mass is above ~100 $M_\odot$ are very hot and encounter pair instability (**Figure 1**) after central C burning (e.g., References 22 and 44 and references therein) at $T \sim 10^9$ K. Gravitational instability occurs because the formation of e^+e^- pairs from high-energy photons converts thermal energy to rest-mass energy and thereby reduces the adiabatic index of the EoS to below 4/3.

For stars whose mass ranges between ~100 $M_\odot$ and ~140 $M_\odot$, and for $M_* \gtrsim 260$ $M_\odot$, collapse to a BH is expected. For intermediate masses, the ignition of the still-available thermonuclear fuel during the implosion is violent enough to trigger the complete disruption of the star with an explosion energy up to more than 10^{53} erg and the production of up to $\gtrsim 50$ $M_\odot$ of ^{56}Ni (22, 44). Although such thermonuclear CCSNe were originally termed HNe by Woosley & Weaver (45), they are now commonly referred to as pair-instability SNe (PISNe) or pair-capture SNe (PCSNe). In the case of BH formation, especially in the presence of rotation that allows for an accretion torus, huge amounts of energy (roughly 0.01–0.03 $M_*c^2 \sim 10^{55}$ erg) are released in neutrinos, depending on the angular momentum (46).

Whereas some recently discovered ultrabright SNe and transients (e.g., SNe 2002ic, 2005gj, 2005ap, 2006gy, 2007bi, 2008es, 2010gx) have been discussed as PISN candidates (e.g., References 47 and 48), other explanations for the extreme luminosity than excessive Ni yields have been proposed, such as interactions between explosion ejecta and a dense circumstellar medium (49), as well as additional energy release by magnetar spin-down (50). The expected rate of PISNe is small—perhaps 1 in 100 to 1,000 normal stellar core collapses—and presumably is associated mostly with metal-poor host galaxies. In the Milky Way, perhaps two dozen very massive hypergiants, such as the evolved luminous blue variable star η Carinae, could end their lives in such events. Although the nature of the stellar death events associated with ultrabright transients and, in particular, the energy source of their extraordinary luminosity are not at all clear and will remain a topic of intense research and debate, space limitations require us to focus this review on the physics and processes that are relevant for the vast majority of ordinary CCSNe.

3. NUMERICAL MODELING AND PHYSICS INGREDIENTS

During the two decades that followed the pioneering work by Colgate & White (6), Arnett (63), and Wilson (64), SN modeling was constrained to spherically symmetric (one-dimensional) simulations, with only a few exceptions (65–68); during the post–SN 1987A era, however, the situation has radically changed. Detailed observations of SN 1987A in the era of modern astronomy revealed that large-scale mixing processes had transported radioactive nuclei with velocities up to ~4,000 km s^{-1} from the deep core far into the H envelope of the exploding star. These findings suggested that spherical symmetry had already been broken during the very first moments of the blast (69, 70). Moreover, two-dimensional (2D) simulations performed in the early 1990s demonstrated that violent convective overturn takes place in the neutrino-heating layer between the gain radius and the stalled accretion shock (8–11). This result raised hopes that buoyant energy transport to the shock could crucially support the delayed neutrino-heating mechanism and could finally ensure robust explosions after 1D models proved successful only by making special assumptions that could not withstand closer, more detailed analysis. For example, neutron-finger

instability inside the nascent NS was proposed to enhance the neutrino luminosities and thus neutrino heating (71), but this hypothesis is now disfavored because lepton equilibration between fingers and surroundings was found to proceed faster than thermal equilibration (13, 72).

Below, we summarize more recent developments and the present status of numerical approaches. Although three-dimensional (3D), general relativistic (magneto-)hydrodynamic simulations—including microphysical EoSs and sophisticated, energy-dependent neutrino transport—are the ultimate objective, only preliminary work in this direction has been performed. Mastering this grand computational challenge will require highly parallelized codes with excellent scaling capability on tens of thousands of processor cores to achieve sustained performance on the level of hundreds of teraflops to petaflops per second. Still, a single 3D model calculation will require several weeks to months.

3.1. Hydrodynamics and Gravity

To date, fully self-consistent modeling of stellar collapse and explosion in 3D has been achieved only by Fryer & Warren (73, 74) and Fryer & Young (75), but they had to sacrifice many aspects of the modeling that are important for quantitatively reliable and conclusive results concerning the SN mechanism. In particular, Newtonian gravity and a gray, flux-limited neutrino diffusion (FLD) scheme (8) were applied in combination with a smoothed particle hydrodynamics (SPH) method, which permits economical calculations in 3D with relatively low resolution but is noisy and diffusive. Good resolution and an accurate representation of the hydrodynamical quantities, however, are essential components for treating the growth of fluid instabilities from initial seeds in the SN core (76, 77). Also, the use of general relativity (GR) and a multigroup (MG) description of neutrino transport, including velocity-dependent observer corrections, caused important differences in 1D (78, 79) and 2D simulations (80, 81).

Other groups, which used mesh-based discretization schemes for solving the hydrodynamics, have studied more constrained problems in 3D and have made even more radical approximations of the relevant (micro)physics. For example, the development of a nonradial hydrodynamic instability of the accretion shock in a collapsing stellar core, the so-called standing accretion shock instability (SASI) (84), has been investigated (82, 83) for a steady-state flow through outer and inner grid boundaries with an ideal-gas EoS and parameterized neutrino-cooling terms. A similar accretion setup with a microphysical EoS and additional simple neutrino-heating terms for prescribed luminosities and spectra [neutrino lightbulb approximation (NLA)] has also been studied (85, 86); this setup enabled neutrino-driven convection. Using the NLA, Nordhaus et al. (87) and Hanke et al. (88) systematically investigated the onset of an explosion in "realistic" collapsing stellar cores by varying the driving neutrino luminosity to explore the dependence on the dimension(s) (1D, 2D, or 3D) of the simulation. GW signals from the infall, core-bounce, and early-postbounce (∼100-ms) phases were computed with 3D GR for NS and BH formation (89, 90), as well as with 3D Newtonian hydrodynamics and an effective general relativistic potential [developed as an approximation of GR gravity (91, 92)], for NS formation (93). These computations resulted in various crude simplifications of the neutrino effects and partly of the EoS of the stellar plasma.

A gray description of the neutrino transport outside of an excised high-density core of the proto–neutron star (PNS) (94) has been used to explore NS kicks, neutrino emission asymmetries, and GW signal characteristics through long-time 3D simulations of SN explosions (95, 96). The first results from Newtonian 3D calculations with more detailed MG transport treatments have been published; these calculations employed either ray-by-ray (RbR) MG FLD (97) or an implementation of the isotropic diffusion source approximation (Section 3.2) for ν_e and $\bar{\nu}_e$ with (98) and without (99) an RbR approach, coupled to a trapping treatment for heavy-lepton neutrinos.

3.2. Neutrino Transport

Over the past decade, sophisticated multi–energy group solvers for three-flavor neutrino transport, including energy-bin coupling and velocity-dependent terms (corrections due to the motion of the stellar plasma), have been developed and applied to all stages of stellar core collapse and the transition to explosion in 1D calculations. This feat was achieved through direct integration of the Boltzmann transport equation (BTE) with a discrete-ordinate (S_N) method in GR simulations (100, 101) and through integration of the set of two-moment equations of the BTE for neutrino number, energy, and momentum by use of a variable Eddington-factor closure obtained from convergent iteration with a model (i.e., simplified) Boltzmann equation. The latter approach was developed for Newtonian (91, 102) and GR simulations (103). It was also generalized for multidimensional applications through the adoption of an RbR+ approximation (80, 91), in which spherical transport problems are solved on each angular bin of a 2D or 3D polar coordinate grid. This approximation implies that the neutrino intensity is assumed to be axially symmetric around the radial direction and that the neutrino flux is considered to be purely radial. The plus sign signals, however, that neutrino pressure gradients and the lateral advection of neutrinos with fluid flows are taken into account in the optically thick regime to prevent artificial hydrodynamic instabilities (80).

All the 1D and 2D SN models published by the Garching group (e.g., References 80 and 104–107) include the full state-of-the-art set of neutrino interactions listed in **Table 1**. Recently, 1D results based on a similarly refined treatment of the neutrino processes were published by the Oak Ridge group (79).

So far, truly multidimensional, energy-dependent transport schemes for radiation hydrodynamics with neutrinos have been extensively used in 2D Newtonian simulations only by an

Table 1   Neutrino reactions with stellar medium particles and between neutrinos in the Garching models

Process	Reference(s)
β processes	
$\nu_e + n \rightleftharpoons e^- + p$	51[†]
$\bar{\nu}_e + p \rightleftharpoons e^+ + n$	51[†]
$\nu_e + (A, Z) \rightleftharpoons e^- + (A, Z + 1)$	55
Scattering reactions	
$\nu + (A, Z) \rightleftharpoons \nu' + (A, Z)$	56 (ion-ion correlations)
	57 (inelastic contributions)
$\nu + N \rightleftharpoons \nu' + N$	51[†]
$\nu + e^{\pm} \rightleftharpoons \nu' + e^{\pm}$	58
("Thermal") pair production	
$\nu + \bar{\nu} \rightleftharpoons e^- + e^+$	59, 60
Nucleon-nucleon bremsstrahlung	
$\nu + \bar{\nu} + N + N \rightleftharpoons N + N$	61
Reactions between neutrinos	
$\nu_{\mu,\tau} + \bar{\nu}_{\mu,\tau} \rightleftharpoons \nu_e + \bar{\nu}_e$	62
$\nu_x + \{\nu_e, \bar{\nu}_e\} \rightleftharpoons \nu_x' + \{\nu_e', \bar{\nu}_e'\}$	62

N means either n or p, $\nu \in \{\nu_e, \bar{\nu}_e, \nu_\mu, \bar{\nu}_\mu, \nu_\tau, \bar{\nu}_\tau\}$, and $\nu_x \in \{\nu_\mu, \bar{\nu}_\mu, \nu_\tau, \bar{\nu}_\tau\}$. In addition to inelastic nucleon recoil, thermal motions, phase-space blocking, high-density nucleon-nucleon correlations (51) and weak magnetism corrections (52), quenching of the axial-vector coupling (53) and the reduction of the effective nucleon mass at high densities (54) are taken into account in the rates marked with a dagger symbol. A prime symbol indicates that the neutrino can exchange energy with the scattering target (nonconservative or inelastic scattering).

Arizona–Jerusalem–Princeton (AJP) collaboration, which applied a MG FLD method (e.g., References 108–110) and an S_N solver for a multiangle treatment (111, 112). However, this collaboration did not use energy-bin coupling and did not properly account for effects associated with fluid motions. These are severe shortcomings (79, 80), which have been avoided in more elaborate 2D Newtonian implementations of both MG FLD (113) and a two-moment closure scheme for the coupled set of neutrino energy and momentum equations (114). An alternative approach is the isotropic diffusion source approximation (115), in which the neutrino distribution function is decomposed into trapped and streaming particle components whose separate evolution equations are coupled by a diffusion source term. This method was simplified to an RbR version for ν_e and $\bar{\nu}_e$ and only a subset of neutrino processes in 2D (116) and 3D (98) SN simulations. A more detailed comparison between and critical assessment of presently employed transport treatments can be found in Reference 79.

Future work in 3D time-dependent neutrino transport in radiation-hydrodynamics calculations has been outlined in the form of a rigorous solution of the 6+1-dimensional BTE (three spatial dimensions, energy, and two direction angles for the radiation momentum, plus time) by an S_N discretization scheme (117), by spectral methods (118), and in GR by a truncated moment formalism (119). However, observer corrections due to fluid motion, relativistic effects, nonlinear energy-coupling interaction kernels, and high parallelization efficiency are major challenges.

Direct comparisons between multidimensional SN calculations performed by different groups with different codes and approximations have not yet been carried out, in contrast to the 1D case (103, 120). Such comparisons pose a formidable challenge. However, compared with a multiangle (S_N) treatment (111), FLD underestimates angular variations of the radiated neutrinos and sphericizes the radiation field, although fundamental changes in the hydrodynamic evolution were not observed despite higher neutrino-heating rates with the S_N code. On the contrary, the RbR approximation generically sharpens angular variations because all fluxes are radial. Local emission maxima (i.e., hot spots) in the neutrinospheric region therefore send radiation only in the radial direction. Nevertheless, because nonspherical accretion flows in the SN core exhibit unsteady behavior in space and time (e.g., Reference 96), so-called variational averaging can be expected to diminish any dynamical consequences of local emission peaks (80). The complexity and computational intensity of neutrino-hydrodynamics will require the use of simplifications in the foreseeable future.

3.3. Equation of State and Composition of Stellar Plasma

The nuclear and subnuclear EoSs are important ingredients for SN modeling. Unfortunately, our knowledge of the supranuclear regime, in particular, is incomplete, although information from nuclear theory and experiments (122) as well as from astrophysical observations [for example, the recently discovered 1.97-$M_\odot$ binary millisecond pulsar PSR J1614-2230 (123)] is rapidly increasing and is beginning to set serious constraints on the possible existence of larger mass regions with exotic phases in NS interiors (124, 125).

The two EoSs for hot NS matter that have been widely used for stellar core collapse over the past decade are those of Lattimer & Swesty (126) and Shen et al. (127). Both EoSs include nucleons and nuclei, electrons and positrons, and photons. The former is based on a compressible liquid drop model (128) with a Skyrme force for nucleon interactions. The transition to homogeneous nuclear matter was established by a Maxwell construction. Most of the SN simulations by the Garching group were performed with a version of the EoS (LS180-EoS) that had an incompressibility modulus of bulk nuclear matter of $K = 180$ MeV and a symmetry energy parameter of 29.3 MeV. The Shen et al. EoS (STOS-EoS) employed a relativistic mean field model with parameter settings that reproduce the characteristic properties of heavy nuclei. This EoS was

extended with the Thomas–Fermi spherical-cell approximation to describe homogeneous matter as well as inhomogeneous conditions. Its bulk incompressibility and symmetry energy have values of 281 MeV and 36.9 MeV, respectively.

These EoSs describe the nuclear composition as a mix of free nucleons, α particles, and a representative heavy nucleus, whose mass and charge numbers depend on density, temperature, and neutronization of the matter. Although largely different mass and charge numbers are returned by both EoSs during the infall stage and affect, for example, neutrino trapping through coherent neutrino-nuclei scatterings, 1D simulations yield basically the same behavior. Quantitative differences occur only on the modest level of 5% to 25% in quantities characterizing collapse, bounce, and early postbounce evolution, for instance, in the central lepton fraction at neutrino trapping, the position of shock formation, the peak luminosity of the ν_e burst, and the maximum radius to which the shock expands before it retreats again (17, 129–131). This outcome is even more astonishing in view of the appreciably different adiabatic index $\Gamma = (\partial \ln P / \partial \ln \rho)_s$ (where P, ρ, and s are pressure, density, and entropy per nucleon, respectively) for both EoSs around nuclear density ($\Gamma_{LS} \sim 2.2$; $\Gamma_{STOS} \sim 2.9$) and the correspondingly different maximum compression and rebound behavior at bounce. Mazurek's law applies; according to this law, the effects of any change in the microphysics on collapsing stellar cores are moderated by strong feedback between the EoS, weak interactions, neutrino transport, and hydrodynamics (132).

To achieve a more elaborate treatment of the nuclear composition in the shock-heated region below neutrinospheric densities after bounce and to connect smoothly to the chemical abundances of the progenitor star, the Garching simulations employed, at $\rho < 10^{11}$ g cm^{-3}, a Boltzmann-gas NSE description with typically two dozen nuclear species and, in the non-NSE regime at $T \lesssim 5 \times 10^9$ K, a nuclear "flashing" treatment (91) or, also available, a small reaction network for nuclear burning.

With a maximum gravitational mass of 1.83 $M_\odot$ for cold NSs in weak equilibrium, the LS180-EoS is not compatible with PSR J1614-2230. Moreover, an incompressibility of $K = 180$ MeV seems to conflict with the experimentally favored value of $K \sim 240$ MeV for symmetric nuclear matter (133, 134). Whereas the STOS-EoS ($M_{max}^{STOS} \approx 2.22$ $M_\odot$) fulfills both constraints, its radius of ~ 15 km for a 1.4-$M_\odot$ NS does not match the best NS radius estimate from the currently most comprehensive evaluation of astrophysical data: $R_{NS} \sim 11$–12.5 km for $M_{NS} = 1.4$ $M_\odot$ (125). This estimate overlaps with the range deduced from theoretical considerations (122), ~ 10 to 14 km, which in turn agrees with an NS radius of ~ 12 km for the LS180-EoS.

The properties of cold, neutronized NSs, however, are not necessarily conclusive for the conditions in the hot SN-core environment. Indeed, for different versions of the LS-EoS with $K = 180$, 220, or 375 MeV (the last two of which are compatible with the mass value for PSR J1614-2230), the structure of hot PNSs well below the maximum mass (which is relevant for the early postbounce evolution of collapsing stellar cores) shows only smaller differences. Correspondingly, 1D core-collapse simulations with these EoS versions revealed only minor differences until hundreds of milliseconds after bounce (130, 135, 136). During the later PNS cooling phase, and especially when mass accretion brings the PNS close to the mass limit, differences in the stiffness and the symmetry energy of the EoS can have important consequences, for instance, for the time when BH formation occurs (131) or for convective activity in the PNS and its influence on the neutrino emission (137). Moreover, 2D simulations showed (106; A. Marek & H.T. Janka, manuscript in preparation) that the explosion of 11.2-$M_\odot$ and 15-$M_\odot$ progenitors depends sensitively on the radius evolution of the PNS in the first few hundred milliseconds after bounce (i.e., the radius contraction of the PNS, in contrast to the final radius of the NS) because a more rapidly shrinking remnant radiates neutrinos with higher fluxes and energies (17, 129, 131, 213). This process enhances neutrino heating and, in particular, enables more violent hydrodynamic instabilities (**Figure 4**).
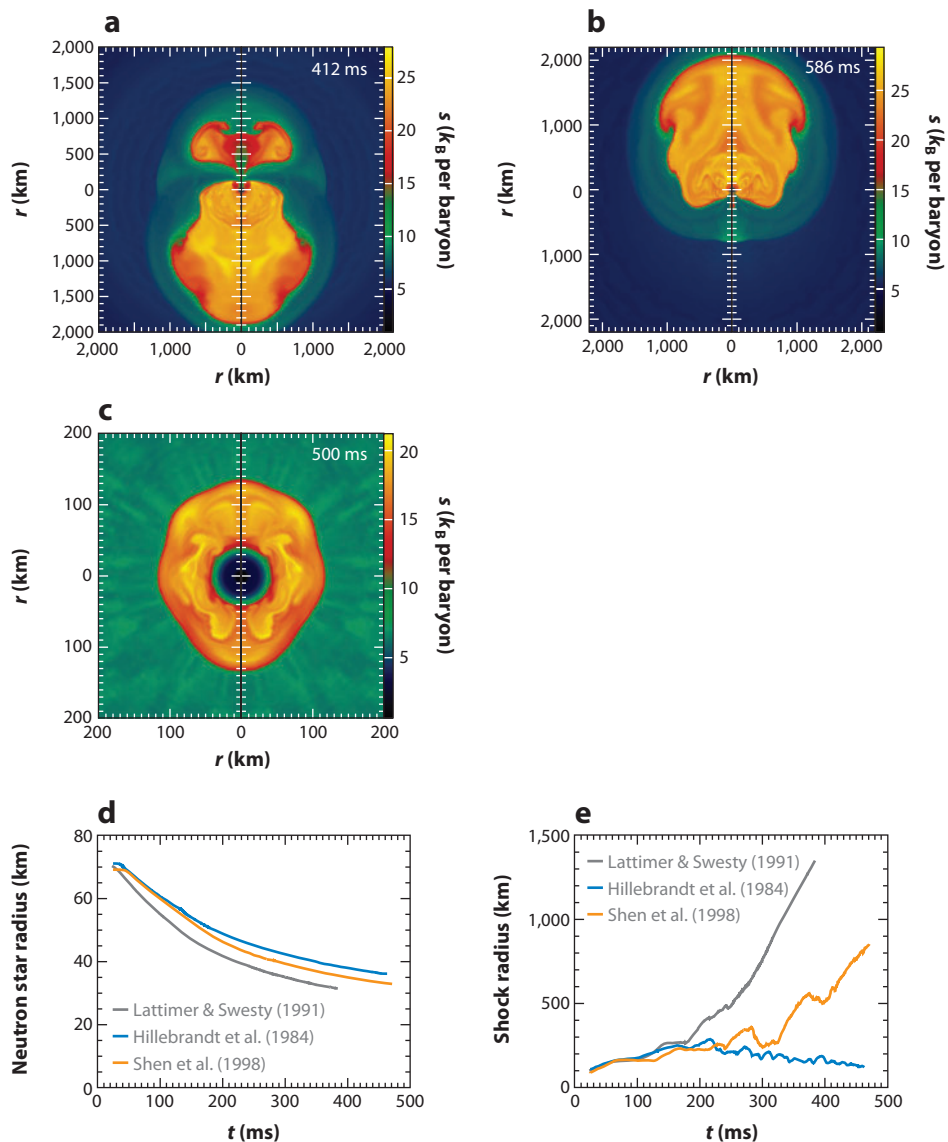
Figure 4

Two-dimensional supernova (SN) simulations (A. Marek & H.T. Janka, manuscript in preparation) of an 11.2-$M_\odot$ star (22) for three different nuclear equations of state (EoSs). (*a–c*) Cross-sectional entropy distributions for (*a*) the Lattimer & Swesty (126) EoS at 412 ms after bounce, (*b*) the Shen et al. (127) EoS at 586 ms after bounce, and (*c*) the Hillebrandt et al. (121) EoS at 500 ms after bounce. The last is the stiffest EoS of the set. It leads to the slowest contraction of the proto–neutron star (*d*) and, because of weaker neutrino heating and less vigorous hydrodynamic mass motions, does not yield an explosion within the simulated time, as is visible in the evolution of the average shock radius (*e*).

Various new nonzero-temperature EoSs for SN studies have recently been published (138–141). Now that modern 1D SN codes are available, these EoSs have been (or will be) channeled through an "industrial" testing pipeline, which has confirmed (or probably will confirm) the modest influence of differences near or above nuclear-matter density on the early shock evolution in 1D, as has been reported in earlier and recent studies (131, 135, 136). Also, a refined description of the nuclear composition (131, 138) has not manifested itself in a big impact on infall and shock formation. Future studies, also in 2D and 3D, must show whether light nuclei that have so far been ignored (^2H, ^3H, ^3He, Li), in addition to ^4He (142–144), will have any relevant effects on the SN mechanism (131, 142) or on the neutrino-driven wind from the cooling PNS (145).

4. EXPLOSION MECHANISMS

In this section, we review the mechanisms by which the gravitational binding energy of the collapsing stellar core can be tapped to eject the outer stellar layers in a SN blast. A particular problem in understanding the onset of the explosion of massive stars is connected to the need to reverse implosion to explosion by transferring energy from the nascent NS to the overlying shells. This situation is different from that for thermonuclear SNe (type Ia SNe) of WDs, in which the combustion (by deflagration or detonation) of C and O to Ni and Si in an essentially hydrostatic object releases sufficient energy to unbind and destroy the whole star.

The typical energy scale of the explosion of a WD near its Chandrasekhar mass limit is set by the release of nuclear binding energy associated with the conversion of $\sim 1 M_\odot$ of C and O to Si and Ni (roughly 2×10^{51} erg) minus the gravitational binding energy of the initial, highly degenerate WD (several 10^{50} erg). But what sets the energy scale of CCSNe? Why do most "normal" cases have explosion energies similar to those of type Ia SNe? The answer to this question is connected to the initial state of the dying star, in which the gravitationally unstable Fe core is a configuration resembling a massive, degenerate WD, surrounded by dense shells whose gravitational binding energy is of the same order of magnitude, namely around $(1–15) \times 10^{50}$ erg.

Any self-regulated mechanism for powering the explosion deposits an energy in this range, possibly a few times the above value, before the energy transfer is turned off. The neutrino-heating mechanism is such a self-regulated process because the matter particles absorbing energy from neutrinos react by expanding away from the heating region as soon as they acquire an energy of the order of their binding energy. This process evacuates the heating region and diminishes further energy input. However, core-collapse events are very diverse in terms of kinetic energy, ranging from $\gtrsim 10^{50}$ erg to approximately 10^{51} erg for SNe and up to several 10^{52} erg for HNe (**Figure 3**). Explosion energies that greatly exceed the initial gravitational binding energy of the ejecta suggest a driving mechanism other than neutrino heating, a process without the self-regulation described above. Magnetorotational explosions fulfill this requirement because the blast-wave energy is extracted from the huge reservoir of rotational energy of a rapidly spinning PNS by magnetic fields and can be delivered in the form of electromagnetic energy.

Below, we summarize the status of our present understanding of both of these mechanisms. We also address other, more controversial suggestions.

4.1. Thermonuclear Mechanism

Although ignition of thermonuclear combustion in compression-heated, free-falling shells cannot blow matter outward (6), Russian scientists (147–150) proposed that neutrino radiation from the collapsing stellar core heats the degenerate C and O shell of a low-mass progenitor star at hydrostatic conditions and at a density around 2×10^9 g cm^{-3}, thereby igniting a thermonuclear
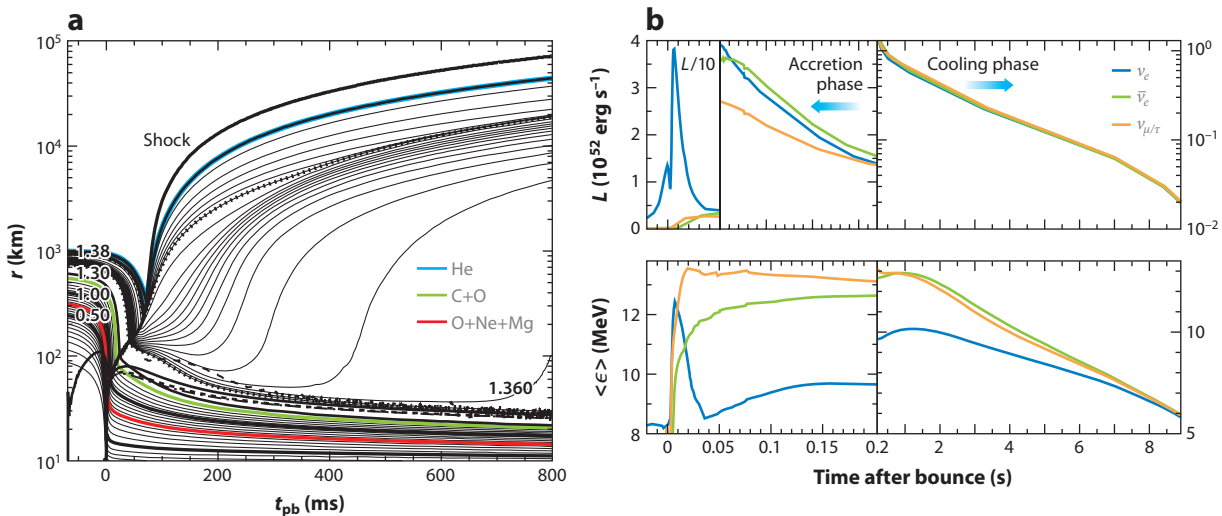
Figure 5

(*a*) Neutrino-powered electron-capture supernova (ECSN) of an 8.8-$M_\odot$ star with an O-Ne-Mg core (21, 28), visualized by mass-shell trajectories of a one-dimensional simulation (105). The SN shock (*bold*, *outgoing line*) expands for ~50 ms as an accretion shock (the downstream velocities are negative) before it accelerates by reaching the steep density gradient at the edge of the core. Neutrino heating subsequently drives a baryonic "wind" off the proto–neutron star (PNS) surface. Colored lines mark the inner boundaries of the Mg-rich layer in the O-Ne-Mg core (red; ~0.72 $M_\odot$), the C-O shell (green; ~1.23 $M_\odot$), and the He shell (blue; ~1.38 $M_\odot$). The outermost dashed line indicates the gain radius, and the inner solid, dashed, and dash-dotted lines represent the neutrinospheres of ν_e, $\bar{\nu}_e$, and ν_x, respectively. (*b*) Neutrino luminosities and mean energies from an ECSN for the infall, ν_e breakout burst, accretion phase, and PNS cooling evolution (107). The average energies are defined as the ratio of energy to number fluxes. Panel *a* reproduced with permission from ESO.

burning front that explodes the star. The heating was considered to occur mainly by neutrino-electron scattering.

Although this is an appealing idea, neither the stellar nor dynamical conditions assumed for this scenario could be verified by detailed progenitor and explosion models. In, for example, O-Ne-Mg-core progenitors, which define the low-mass limit of stars that undergo core collapse to radiate large neutrino luminosities, the C and O shell is initially located between roughly 500 and 1,000 km (at densities $\lesssim 4 \times 10^8$ g cm^{-3}) and falls dynamically inward (with compression-induced burning) long before it is exposed to a high fluence of neutrinos (**Figure 5**). If, in contrast, the O and C layers are farther out at $r > 1,000$ km, as in more massive Fe-core progenitors (**Figure 2**), then the neutrino flux is diluted by the large distance from the source, and the electron densities (and degeneracy) there are much lower than those adopted by the Russians (147–150). Therefore, neutrino-electron scattering cannot raise the temperature to the ignition threshold.

Presently, PISNe are the only stellar core-collapse events wherein the explosion mechanism is known to be based on thermonuclear energy release (Section 2.4). However, a closer examination of the possibility of neutrino-triggered burning in the significantly more compact low-metallicity stars might be interesting.

4.2. Bounce-Shock Mechanism

The purely hydrodynamical bounce-shock mechanism (4, 5), in which the shock wave launched at the moment of core bounce (Section 2.2) causes the prompt ejection of stellar mantle and

envelope, was the subject of intense research in the 1980s (for a review, see Reference 151). However, since then, detailed analytical analyses of collapse and bounce physics (e.g., Reference 152 and references therein), as well as all modern core-collapse simulations (despite continuous improvements and significant quantitative differences in details, linked mainly to important refinements of electron captures on heavy nuclei and neutrino-electron scattering during infall), agree in their basic outcomes: The prompt mechanism cannot cause the explosion of any progenitor star.

Upgrades of the microphysics turned out to disfavor prompt explosions by decreasing the size of the homologously and subsonically collapsing inner core, whose mass scales with the instantaneous Chandrasekhar mass, $M_{\mathrm{Ch}}(t) \propto Y_e^2(t)$, and whose edge defines the location of shock formation at bounce. [The number fraction Y_i of particles, here electrons (e), is defined as the number of particles per nucleon.] With the present, most sophisticated treatment of neutrino emission by electron captures on nuclei and free protons during core infall (55), the central electron fraction $Y_{e,\mathrm{c}}$ decreases, after neutrino trapping, to 0.25 to 0.27 (which corresponds to a trapped lepton fraction of 0.285 to 0.300). The shock-formation point (defined by the location where the entropy first reaches 3 k_{B} per nucleon) lies at an enclosed mass of only 0.4 to 0.5 $M_\odot$ (17, 104, 153). Moreover, because the preferred nuclear EoSs are relatively stiff, the rebound of the inner core is too weak to transfer a large energy to the shock. The flow discontinuity, running into supersonically infalling material at densities below $\sim 10^{13}$ g cm^{-3}, quickly loses its initial energy by heating the plasma to entropies of several k_{B} per nucleon and thereby disintegrating heavy nuclei into free nucleons (which consumes roughly 1.7×10^{51} erg per 0.1 $M_\odot$). A short transient period of positive postshock velocities therefore lasts only 1 to 2 ms, after which the velocity in the whole postshock region becomes negative again. A negative postshock velocity defines the moment of shock stagnation, at which time the shock has traveled through only 0.3–0.35 $M_\odot$ of Fe material and is still deep inside the stellar Fe core. Because at this point the preshock density is still above 10^{11} g cm^{-3}, shock stagnation happens well before shock breakout and thus before the release of the prompt burst of ν_e. Therefore, lepton number and energy ($\sim 2 \times 10^{51}$ erg) drain by the escape of the ν_e burst do not cause the shock stagnation.

Despite negative velocities and thus accretion flow to the central NS in the downstream region of the shock, the latter continues to propagate outward in mass as well as radius. This motion of the shock-stagnation radius is a response to the massive accretion of infalling matter (initially with a rate $\dot{M} \gg 1\ M_\odot\ \mathrm{s}^{-1}$) (**Figure 5**), which emits energy and lepton number in neutrinos and thereby settles onto the PNS only gradually, creating the postshock pressure that pushes the shock position outward. Finally, after reaching a maximum radius of typically 100 to 150 km, the accretion shock again retreats in 1D models, following the contraction of the nascent NS roughly according to the relation

$$R_{\mathrm{s}} \propto \frac{(L_\nu \langle \epsilon_\nu^2 \rangle)^{4/9} R_{\mathrm{NS}}^{16/9}}{\dot{M}^{2/3} M_{\mathrm{NS}}^{1/3}} \propto \frac{R_{\mathrm{NS}}^{8/3}(k_{\mathrm{B}} T_\nu)^{8/3}}{\dot{M}^{2/3} M_{\mathrm{NS}}^{1/3}} \propto \frac{L_\nu^{4/3}}{\dot{M}^{2/3} M_{\mathrm{NS}}^{1/3}(k_{\mathrm{B}} T_\nu)^{8/3}}, \qquad 2.$$

which can be derived by combining equations 33, 39, 43, 44, 56, and 63 of Reference 154 and assuming that $R_{\mathrm{g}} \propto R_{\mathrm{NS}}$ for the so-called gain radius R_{g} (see the next paragraph and Section 4.3) and that $L_\nu \propto R_{\mathrm{NS}}^2 T_\nu^4$ and $\langle \epsilon_\nu^2 \rangle \propto (k_{\mathrm{B}} T_\nu)^2$ for neutrino ($\nu \in \{\nu_e, \bar{\nu}_e\}$) luminosity and mean squared energy, respectively. The radius of maximum shock expansion at this stage is still well below the dissociation radius of Fe, for which the equality $GM_{\mathrm{NS}} m_{\mathrm{u}}/R_{\mathrm{diss}} = 8.8$ MeV (where m_{u} is the atomic mass unit) yields $R_{\mathrm{diss}} \approx 200$ km. Thus, the matter behind the shock is fully disintegrated into neutrons and protons.

It is during this $\sim$100-ms period of slow shock expansion that the gain radius emerges, at which energy losses by neutrinos for $r < R_{\mathrm{g}}$ change to neutrino heating for $r > R_{\mathrm{g}}$ (7). Before this moment, neutrino losses dominate in the whole postshock layer. The onset of neutrino-energy

deposition also allows convective activity to develop behind the shock: Neutrino heating creates a negative entropy gradient, ds/dr, which is unstable in the strong gravitational field according to the Ledoux criterion:

$$C_{\mathrm{L}} = \left(\frac{\partial \rho}{\partial s}\right)_{Y_e, P} \frac{ds}{dr} + \left(\frac{\partial \rho}{\partial Y_e}\right)_{s, P} \frac{dY_e}{dr} > 0. \qquad 3.$$

This criterion, however, exactly defines growth conditions for convection and Rayleigh–Taylor structures only for a static layer; it needs to be generalized for the infalling flow in the postshock region (76, 104, 155). Convective activity can take place there only when the inward advection timescale, $t_{\mathrm{adv}} \sim r/|v_r|$ for radial velocity v_r, is sufficiently longer than the convective growth timescale of perturbations (inverse Brunt–Väisälä or buoyancy frequency), $t_{\mathrm{conv}} \sim (g_{\mathrm{grav}}|C_{\mathrm{L}}|/\rho)^{-1/2}$, or longer than the buoyancy acceleration timescale, $t_{\mathrm{buoy}} \sim [g_{\mathrm{grav}}(\delta\rho/\rho)/r]^{-1/2}$, of blobs with density contrast $\delta\rho/\rho$ in a local gravitational field with acceleration $g_{\mathrm{grav}} = GM/r^2$ (155, 156). The breaking of spherical symmetry by hydrodynamic instability, which manifests itself in the growth of initially small, random seed perturbations to large-scale structures, is generic to the shock-stagnation phase in collapsing stellar cores and is decisive for the success of the neutrino-heating mechanism and for the further destiny of the stalled accretion shock.

4.3. Neutrino-Heating Mechanism

The development of a neutrino-heating layer is a natural consequence of the contraction of the PNS and the associated compactification of its surrounding accretion layer during the postbounce accretion phase. The contraction of the PNS leads to increasing neutrinospheric temperatures and therefore growing mean energies of the radiated neutrinos (**Figure 7**). The more energetic neutrino emission, together with the decreasing postshock temperature at larger shock radii, allows for the appearance of a gain radius: Because the temperature in the postshock layer drops roughly as r^{-1} (this condition is well fulfilled for convectively mixed, isentropic conditions, whereas in 1D the gradient is even steeper), the neutrino-cooling rate per nucleon by captures of (nondegenerate) e^- and e^+ on protons and neutrons drops with $q_\nu^- \propto T^6 \propto r^{-6}$. In contrast, the neutrino-heating rate per nucleon (which is dominated largely by ν_e and $\bar{\nu}_e$ absorption on free neutrons and protons, respectively) scales with $q_\nu^+ \propto L_\nu \langle \epsilon_\nu^2 \rangle r^{-2}$. This rate therefore decreases less steeply with r than q_ν^- does, which allows a crossing point, R_{g}, to occur (7); here, $T_{\mathrm{g}}^3 R_{\mathrm{g}} \propto \sqrt{L_\nu \langle \epsilon_\nu^2 \rangle}$.

4.3.1. Heating efficiency and energetics. Given a density profile $\rho \propto r^{-3}$ between gain radius R_{g} and shock R_{s} (e.g., Reference 154), a preshock (free-fall) velocity $v_0 = -\sqrt{2GM_{\mathrm{NS}}/R_{\mathrm{s}}}$, a mass infall rate $\dot{M} = 4\pi R_{\mathrm{s}}^2 |v_0|\rho_0$ of the progenitor star, and density jump $\beta = \rho_1/\rho_0 \sim 10$ at the shock, the optical depth for ν_e and $\bar{\nu}_e$ absorption in the gain layer can be estimated as

$$\tau \approx 0.026 \left(\frac{k_{\mathrm{B}}T_\nu}{4\ \mathrm{MeV}}\right)^2 \left(\frac{\dot{M}}{0.1\ M_\odot\ \mathrm{s}^{-1}}\right) \left(\frac{R_{\mathrm{s}}}{200\ \mathrm{km}}\right)^{3/2} \left(\frac{R_{\mathrm{g}}}{100\ \mathrm{km}}\right)^{-2} \left(\frac{M_{\mathrm{NS}}}{1.5\ M_\odot}\right)^{-1/2}. \qquad 4.$$

Here, $Y_n \approx Y_p \approx 0.5$ and $\langle \sigma_{\mathrm{abs}} \rangle \approx 3.26 \times 10^{-41}[k_{\mathrm{B}}T_\nu/(4\ \mathrm{MeV})]^2\ \mathrm{cm}^2$ for the average absorption cross section of a blackbody neutrino spectrum with temperature T_ν [therefore, $\langle \epsilon_\nu^2 \rangle \approx 21(k_{\mathrm{B}}T_\nu)^2$]. Equation 4 suggests that for typical accretion rates, $\dot{M} = 0.1$–$0.5\ M_\odot\ \mathrm{s}^{-1}$, several percent of the neutrino luminosity from the neutrinosphere can be absorbed in the gain layer, which accounts for a volume-integrated neutrino-heating rate, $Q_\nu^+ = \tau(L_{\nu_e} + L_{\bar{\nu}_e}) \approx 10^{51}$–$10^{52}\ \mathrm{erg\ s}^{-1}$, for ν_e and $\bar{\nu}_e$ luminosities, L_ν, of a few $10^{52}\ \mathrm{erg\ s}^{-1}$ during the postbounce accretion phase (**Figure 7**).

However, in a dynamical situation, as in the gain layer, where the matter is not at rest, the optical depth (which determines the interaction probability of a crossing neutrino) is not a

perfectly appropriate measure for the heating efficiency. This statement holds in particular in the multidimensional case, wherein accretion funnels carry cold (low-entropy) matter from the shock toward the NS while neutrino-heated matter expands outward in high-entropy bubbles. At such conditions, the residence time of the matter in the gain layer accounts for the duration of its exposure to neutrino heating. Whereas in the 1D case the advection time $t_{adv} \sim (R_s - R_g)/|v_1|$ (where $v_1 = v_0/\beta$) measures how long the accretion flow requires to go from R_s to R_g (156, 157), the dwell time in the gain region is better captured in the multidimensional situation by the more general expression (104, 106)

$$t_{\mathrm{dwell}} \approx \frac{M_g}{\dot{M}}, \quad\quad\quad 5.$$

which relates the mass in the gain layer M_g with the mass accretion rate $\dot{M}$ through the shock and (for conditions near steady state) through the gain radius. With an energy-transfer rate per nucleon by neutrino absorption of $q_\nu^+ = n_\nu \langle \epsilon_\nu \rangle \langle \sigma_{abs} \rangle c$, where $n_\nu \langle \epsilon_\nu \rangle = L_\nu/(4\pi r^2 c)$, each nucleon absorbs an energy of $q_\nu^+ t_{\mathrm{dwell}} \sim 50$ MeV for time $t_{\mathrm{dwell}} \sim 0.1$ s when one assumes that $k_B T_\nu = 4$ MeV, $L_\nu = 3 \times 10^{52}$ erg s^{-1} ($\nu \in \{\nu_e, \bar{\nu}_e\}$), and $r = R_g \sim 100$ km. An energy transfer of 50 MeV per nucleon can produce a temperature of $\sim$3 MeV and an entropy of $\sim$20 k_B per nucleon of an $e^\pm$-photon-dominated plasma at $\rho \sim 10^9$ g cm^{-3} (**Figures 4**, **6**). The total energy deposition rate by ν_e plus $\bar{\nu}_e$ absorption in the gain layer thus becomes

$$Q_\nu^+ = q_\nu^+ \frac{M_g}{m_u} \sim 9.4 \times 10^{51} \frac{\mathrm{erg}}{\mathrm{s}} \left(\frac{k_B T_\nu}{4\,\mathrm{MeV}} \right)^2 \left(\frac{L_\nu}{3 \times 10^{52}\,\mathrm{erg\,s^{-1}}} \right) \left(\frac{M_g}{0.01\,M_\odot} \right) \left(\frac{R_g}{100\,\mathrm{km}} \right)^{-2}. \quad 6.$$

Equation 6 corresponds to a heating efficiency of

$$\frac{Q_\nu^+}{L_{\nu_e} + L_{\bar{\nu}_e}} \sim 0.16 \left(\frac{k_B T_\nu}{4\,\mathrm{MeV}} \right)^2 \left(\frac{M_g}{0.01\,M_\odot} \right) \left(\frac{R_g}{100\,\mathrm{km}} \right)^{-2} \quad\quad 7.$$

and an integral energy deposition of

$$E_N \sim Q_\nu^+ t_{\mathrm{dwell}} \sim 9.4 \times 10^{50} \, \mathrm{erg} \left(\frac{k_B T_\nu}{4\,\mathrm{MeV}} \right)^2 \left(\frac{L_\nu}{3 \times 10^{52}\,\mathrm{erg\,s^{-1}}} \right)$$
$$\times \left(\frac{M_g}{0.01\,M_\odot} \right)^2 \left(\frac{\dot{M}}{0.1\,M_\odot\,\mathrm{s^{-1}}} \right)^{-1} \left(\frac{R_g}{100\,\mathrm{km}} \right)^{-2}. \quad 8.$$

These numbers, reduced by 20% to 30% for neutrino-cooling losses in the gain layer, are compatible with results from detailed simulations (81, 106).

4.3.2. Hydrodynamical explosion models. Neutrino-driven explosions can be found in 1D simulations only for ECSNe of low-mass progenitors (105, 158, 159), considering an 8.8-$M_\odot$ star with an O-Ne-Mg core (21, 28). Because of the extremely steep density gradient at the edge of the O-Ne-Mg core and the corresponding rapid decrease of $\dot{M}$, the radius of the accretion shock increases continuously (Equation 2), thereby creating ideal conditions for neutrino-energy transfer (**Figure 5**). The latter drives a baryonic outflow, which carries the energy for the explosion. The most sophisticated available treatment of neutrino-matter interactions (Section 3.2) (**Table 1**) yielded an explosion energy $E_{O-Ne-Mg} \approx 10^{50}$ erg (105, 158), which was enhanced at most by $\sim$10% in 2D models due to a brief phase ($\sim$50–200 ms after bounce) of convective overturn behind the rapidly expanding shock (33, 158). The low explosion energy and low Ni ejection [several 10^{-3} $M_\odot$ (33)] are compatible with estimates for the Crab SN (Reference 34 and references therein).

For more massive Fe-core progenitors, nonradial hydrodynamic instabilities—convective overturn (8, 9, 11, 73) in combination with SASI activity (84)—are decisive for the success of the neutrino-heating mechanism (104, 106). Whereas 1D models did not explode, the Garching
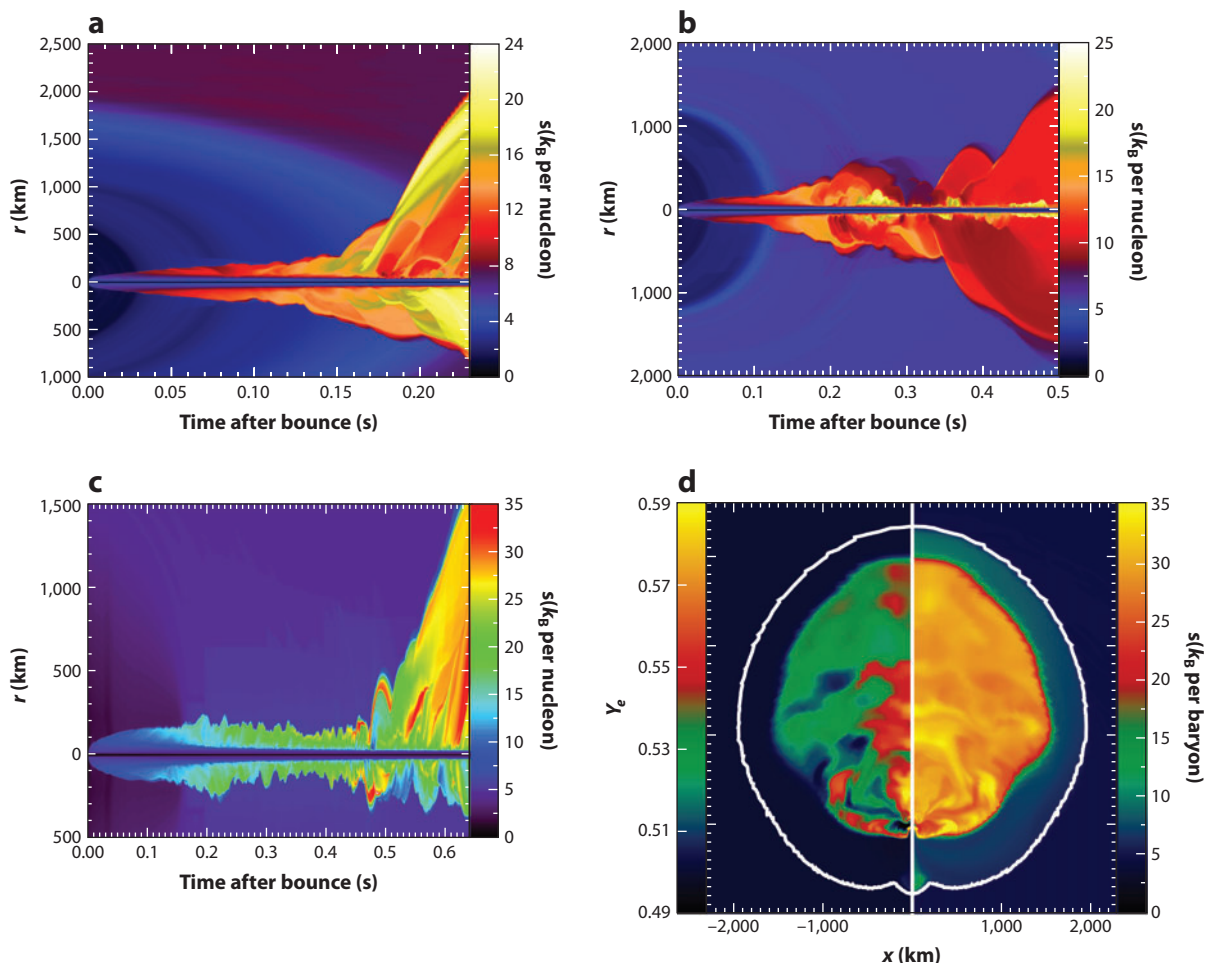
Figure 6

Neutrino-driven explosions of Fe-core progenitors (81, 146). (*a–c*) Time evolution of color-coded entropy profiles in the north and south pole directions for two-dimensional simulations of (*a*) an 8.1-$M_\odot$ ultra-metal-poor (10^{-4} solar-metallicity) star (A. Heger, private communication), (*b*) an 11.2-$M_\odot$ solar-metallicity star (22), and (*c*) a 15-$M_\odot$ solar-metallicity star (23), respectively. The shock position is clearly visible as a sharp boundary between high-entropy (*yellow and red*) and low-entropy (*blue and black*) regions. Shock oscillations are associated with violent convective activity in the neutrino-heating region and strong, bipolar sloshing motions of the whole postshock layer due to the standing accretion shock instability. The explosions develop highly aspherically in all cases. (*d*) An extreme dipole asymmetry of the cross-sectional distribution of electron fraction (Y_e; *left*) and entropy at 775 ms after bounce for the 15-$M_\odot$ model, which explodes in a unipolar way. The neutron star is located at the position of the lowermost long tick mark on the vertical axis, far away from the geometrical center of the roundish shock contour (*white line*).

group found neutrino-driven, although weak, explosions for 11.2- and 15-$M_\odot$ stars in 2D simulations (104, 106). Recently, these results, obtained with the Prometheus-VERTEX program (80, 91), were confirmed by general relativistic 2D simulations (81) based on the newly developed CoCoNut-VERTEX code (103), which also produced explosions for solar-metallicity 27-$M_\odot$ and metal-poor (10^{-4} solar-metallicity) 8.1-$M_\odot$ progenitors with Fe cores (**Figure 6**) (160).

Neutrino-driven explosions for various stars were also observed in 2D and 3D simulations of other groups with different MG treatments of neutrino transport (97–99, 116), whereas the AJP

collaboration observed no success of the neutrino-heating mechanism (108, 109). These findings qualitatively and quantitatively underscore the sensitivity of the outcome to details of the input and methods. Although there are many differences between the modeling approaches in terms of numerics and microphysics, the Garching 2D models in particular include both the full set of neutrino-matter interactions given in **Table 1** and a careful implementation of all fluid-motion-dependent terms, as well as GR effects in the transport. All these effects were recognized to be significant (79, 80) but were simplified or ignored in the AJP calculations due to the omission of energy-bin coupling there (see also Section 3.2). Rather than attribute the conflicting results to transport differences, researchers have repeatedly stated that the success of the Garching simulations is disputable because the unacceptably soft LS180-EoS was used (e.g., Reference 161). This criticism, however, lacks foundation because of the arguments given in Section 3.3 and because the 11.2-$M_\odot$ explosion was reproduced with the stiffer STOS-EoS (**Figure 4**), which did not lead to an explosion in the 11.2-$M_\odot$ run of the AJP collaboration (109).

Self-induced neutrino-flavor conversions in the SN core, which could swap lower-energetic ν_e and $\bar{\nu}_e$ spectra with hotter ν_x and $\bar{\nu}_x$ spectra and therefore could enhance the neutrino heating behind the shock and strengthen the SN explosion, were recently shown not to have an impact during the postbounce accretion phase. Because detailed SN models yield electron densities that are higher than the neutrino densities (mostly $n_e \gg n_\nu$), the matter background dominates and thus suppresses collective neutrino oscillations by dephasing the flavor evolution of neutrinos traveling in different trajectories (162–165).

4.3.3. Effects of nonspherical flows.

Nonradial, turbulent flows increase the residence time of matter in the gain layer (98, 104, 166) and, therefore, the mass M_g in this region (for given $\dot{M}$; Equation 5). This increase leads to a higher total energy-deposition rate by neutrinos, Q_ν^+ (Equation 6), and to an enhanced integral-energy transfer, E_N (Equation 8).

For example, Rayleigh–Taylor fingers, which develop in a convectively unstable situation (Equation 3), channel cool, freshly accreted material from immediately downstream of the shock toward the PNS and thus closer to the gain radius, where neutrino heating is strongest. At the same time, expanding bubbles of buoyant, high-entropy gas allow freshly heated matter to rise away from the gain radius instead of being accreted inward to the cooling layer. This process reduces energy losses by the reemission of neutrinos, which can have important dynamical consequences because cooling for $r < R_g$ is usually much larger than net heating in the gain layer. The combination of all these effects leads to an increase of the temperature and pressure in the gain layer, which in turn pushes the shock farther out. A positive feedback cycle is the result, which for sufficiently strong neutrino heating enables an explosion in the multidimensional case even when the neutrino-driven mechanism fails in 1D.

SASI activity can have similar effects. Not only is the SASI associated with shock expansion and nonradial mass flows, thereby allowing for a larger efficiency of neutrino-energy deposition; it also leads to secondary shocks that dissipate kinetic energy and produce extra heating and higher entropies, strengthening the convective activity and giving additional push to the shock (76, 106).

After the onset of the explosion, the nonspherical situation permits simultaneous shock expansion and ongoing accretion. These effects maintain higher neutrino fluxes and stronger neutrino heating for a longer time, compared with the 1D case (106), where the accretion luminosity decays as soon as shock expansion quenches the mass infall to the PNS.

Although hydrodynamical simulations clearly demonstrate that violent convective and SASI activity is crucial for the success of the neutrino-heating mechanism (160), the nature of the SASI and the exact role of hydrodynamic instabilities and turbulent motions for the onset of the explosion are still a matter of intense research. The SASI—whose amplitude grows from small

pressure and/or entropy perturbations in an oscillatory way, with the highest growth rates for the lowest-order spherical harmonics (dipolar $\ell = 1$ and quadrupolar $\ell = 2$) components (84, 167–169)—seems to be an ideal candidate to explain not only the global asymmetries found in the SN core in simulations but also the large asphericities and mixing effects that are observed in most SNe and SN remnants and that are probably linked to the measured high kick velocities of many young pulsars (Section 6). Linear growth analysis, numerical toy models for the linear and nonlinear regimes (76, 170), and laboratory shallow-water experiments (171) yield evidence that the underlying instability mechanism is an advective-acoustic cycle (172, 173), rather than a purely acoustic one (167).

4.3.4. Runaway threshold. Burrows & Goshy (174) conjectured that the transition to the explosion is a global instability of the postshock layer. By considering steady-state accretion conditions in 1D, they determined a critical neutrino luminosity $L_{\nu,c}(\dot{M})$ as a function of the mass accretion rate that damps shock expansion (Equation 2), above which they found no accretion solutions and thus expected the onset of the explosion. Their reasoning is supported by subsequent, similar analyses of stationary accretion flows (175–177, 177a), as well as by hydrodynamical studies (11, 87, 88, 166, 178).

The existence of a functional relation $L_{\nu,c}(\dot{M})$ as the threshold condition for an explosion can be qualitatively understood by simple analytic considerations. Numerical simulations (104, 106, 166, 178, 179) have shown that the necessary condition for runaway expansion is given by $t_{adv}/t_{heat} > 1$; that is, the explosion can set in when the advection timescale of the mass flow through the gain layer,

$$t_{adv} = \int_{R_g}^{R_s} \frac{dr}{|v_r|} \sim \beta \frac{R_s}{|v_0|} \sim \beta \frac{R_s^{3/2}}{\sqrt{2GM_{NS}}},$$ 9.

exceeds the heating timescale for neutrinos to deposit enough energy to lift matter from a gravitationally bound state to an unbound state. In this context, the total energy of the gas is the relevant quantity, namely the sum of internal, gravitational, and kinetic energies, which in a bound state is negative. By assuming that this energy scales roughly with the gravitational energy near the gain radius, which for a nucleon is $\epsilon_g = -GM_{NS}m_u/R_g$, one obtains

$$t_{heat} \sim \frac{|\epsilon_g|}{q_\nu^+} \propto \frac{M_{NS}R_g}{L_\nu \langle \epsilon_\nu^2 \rangle}.$$ 10.

By setting both timescales to be equal, $t_{adv} = t_{heat}$, and by using Equation 2 for R_s and the fact that R_g follows approximately R_{NS} [that is, $R_g \propto R_{NS} \propto L_\nu^{1/2}/(k_B T_\nu)^2$, which was also applied in deriving Equation 2], one obtains

$$L_{\nu,c}(\dot{M}) \propto \beta^{-2/5}\, \dot{M}^{2/5}\, M_{NS}^{4/5}.$$ 11.

This relation reproduces the functional behavior found in Reference 174 very well [the numerical factor of the scaling relation becomes (5–6) $\times$ 10^{52} erg s^{-1} for $\beta \sim 10$, $\dot{M} = 1\,M_\odot$ s^{-1}, and $M_{NS} = 1.5\,M_\odot$ and slightly varies with the choice of other involved parameters]. Note, however, that the limiting luminosity for steady-state accretion solutions as derived in Reference 174 is usually close to but not identical with the runaway threshold at $t_{adv} > t_{heat}$. This threshold roughly coincides with the time when the fluid behind the shock begins to develop positive total specific energy (see the excellent study in Reference 178).

Numerous studies for both stationary accretion flows (175, 176) and time-dependent conditions in collapsing stellar cores (11, 87, 88, 166) have demonstrated that the critical neutrino luminosity for fixed mass-accretion rate is significantly lowered in the multidimensional case, typically by several tens of percent. The possible (or combined) reasons for this improvement are discussed in

Section 4.3.3, but many aspects are still unsettled. For example, the properties and consequences of neutrino-driven turbulence (e.g., convective energy transport and pressure) are a matter of ongoing research (180), and the effects of 3D hydrodynamics have not yet been clarified. Although there is hope that these effects could make the runaway easier than in 2D (87, 98) and thereby lead to earlier and more powerful explosions, not all studies have revealed a significant reduction of the threshold luminosity in 3D relative to 2D (88). The comparison between 2D and 3D obviously depends on subtle differences in the background flow, neutrino source terms, or even numerics, and it requires further exploration. A sophisticated neutrino transport seems necessary to obtain reliable answers.

4.3.5. Modes of global instability. The results of SN simulations and analytic studies suggest that the onset of an explosion is connected to the global runaway instability of the postshock accretion layer (129, 174), fueled by neutrino energy deposition above a certain threshold (Section 4.3.4). An important question concerns the type of mode that grows fastest to trigger the runaway (178). Unstable oscillatory and nonadiabatic radial modes were observed in many time-dependent 1D simulations—in agreement with linear stability analysis (181)—for neutrino luminosities intermediate between those that are too low to drive explosions and those that suffice to trigger an explosion by the instability of a nonoscillatory radial mode (11, 80, 87, 88, 166, 168, 178, 182). But what happens in the multidimensional case? Is the runaway there caused by an unstable radial oscillatory or nonoscillatory mode, whose development is affected by turbulence altering the conditions of the background flow? Or is a nonradial nonoscillatory (possibly convective) or oscillatory (SASI) mode decisive? Exploration of the growth conditions has only begun, and this research suggests that unstable large-scale, nonoscillatory modes require the highest driving luminosities (181) but that their growth may strongly depend on the conditions in the SN core (160), the dimensionality of the problem, and even a modest rate of rotation (183). Although initial 3D simulations (85, 87, 88, 95, 98, 99) show strongly damped or no radial oscillations, suggesting that SASI modes are less strong in 3D and that the explosion might be connected to unstable nonoscillatory modes (184, 185), none of these simulations were performed with a combination of sufficiently sophisticated neutrino transport, high enough numerical resolution, and consistent inclusion of all dissipative processes (such as the decay of the NS core luminosity, changes in the accretion luminosity, and the shrinking of the nascent NS, all of which provide negative feedback). Final answers will require well-resolved, full-scale 3D radiation-hydrodynamics simulations with reliable neutrino treatment.

4.4. Magnetohydrodynamic Mechanisms

MHD phenomena, in particular the magnetorotational mechanism (MRM) (186, 187), had already been discussed in the 1970s as potential drivers of SN explosions (e.g., References 188 and 189) and were first explored by axisymmetric simulations with approximate microphysics and artificially imposed stellar core-rotation and magnetic field configurations (65, 67). These and a flood of subsequent 2D calculations, which either ignored or radically simplified the neutrino physics (e.g., References 190–193 and references therein) or, more recently, used neutrino transport by MG FLD [assuming, inappropriately, that the stellar medium is at rest (109)], have confirmed that MHD processes, and especially the MRM, are viable agents to extract energy from a highly magnetized NS and to violently expel the outer stellar layers.

Because of the extremely low resistivity of SN matter, magnetic field lines are frozen in the flow. Magnetic flux conservation therefore leads to compressional amplification of the average strength of the nonradial field during core collapse, $B \propto R_{core}^{-2} \propto \rho_{core}^{2/3}$, and a corresponding growth of the

energy density of the magnetic fields ($\propto B^2$). Initial fields, as expected in stellar cores at the onset of gravitational instability, that is, several 10^9 G for the dominant toroidal component (36), can thus increase by a factor of greater than 1,000 but cannot gain dynamically relevant strength, for which the magnetic pressure has to reach a fair fraction of the gas pressure.

Therefore, secondary amplification mechanisms are necessary to further boost the magnetic energy density to values close to equipartition with the stellar plasma. In the MRM, such an increase in energy density can be achieved by tapping the huge reservoir of rotational energy, $E_{rot} \propto J^2_{core}/(M_{core}R^2_{core})$, that builds up at the expense of gravitational energy due to angular momentum (J_{core}) conservation during the infall. The rotational energy in a rapidly spinning PNS with average revolution period P_{NS} thus becomes

$$E_{rot} \sim 2.4 \times 10^{52} \text{ erg} \left(\frac{M_{NS}}{1.5 \ M_\odot} \right) \left(\frac{R_{NS}}{10 \text{ km}} \right)^2 \left(\frac{1 \text{ ms}}{P_{NS}} \right)^2 . \qquad 12.$$

The amplification can occur in one of two ways. It can occur through the wrapping of an (initially present or convectively created) poloidal field, stretching it into a toroidal one, which leads to a linear increase with the number of windings. Alternatively, it can take place by exponential amplification with characteristic timescale of order $4\pi |d\Omega/d \ln r|^{-1}$ [where $\Omega(r) = 2\pi/P_{rot}(r)$ is the angular frequency for the local spin period P_{rot}] through the magnetorotational instability (MRI) (194, 195), whose growth conditions in SN cores have been studied in detail (196). Both processes require differential rotation, which develops naturally during infall. Saturation fields of order

$$B^2 \sim 4\pi\rho r^2\Omega^2 \left(\frac{d \ln \Omega}{d \ln r} \right)^2 \qquad 13.$$

can be expected in an MRI-unstable environment, in which $d \ln\Omega/d \ln r < 0$ must hold to enable the growth of long-wavelength, slow-magnetosonic waves. For sufficiently large angular velocities, fields of order 10^{15}–10^{16} G have been estimated (195).

The ejection of matter can be driven by magnetic pressure and hoop stresses, magnetic buoyancy, or gas heating due to the dissipation of rotational energy through turbulent magnetic viscosity (179, 188, 195). Well-collimated bipolar outflows or jets along the rotation axis, with characteristic power

$$\dot{E}_{MHD} \sim 10^{52} \frac{\text{erg}}{\text{s}} \left(\frac{B}{10^{15} \text{ G}} \right)^2 \left(\frac{r}{30 \text{ km}} \right)^3 \left(\frac{\Omega}{10^3 \text{ rad s}^{-1}} \right), \qquad 14.$$

may be generic (110, 195, 197).

Because the MRM can tap only the free energy of differential rotation in the PNS, $E_{rot}^{free} \ll E_{rot}$, angular velocities near the Keplerian rate of the progenitor core ($P_{core} \sim 1$ s) are required for magnetic fields to grow to dynamical significance. SN simulations (110, 179) suggest that the spin period must be $P_{core} \lesssim 2$–5 s, which leads to NS rotation periods of $P_{NS} \sim (R_{NS}/R_{core})^2 P_{core}$ under the assumption of strict angular momentum conservation. Present stellar evolution models that include angular momentum loss through magnetic breaking, however, yield typical core-rotation periods of $P_{core} \gtrsim 100$ s before collapse (Section 2.2). Such slowly rotating stellar cores are consistent with observed spin rates of newly born WDs (198) and with the estimated spin periods of newly born pulsars of $\sim$10 ms (36, 199), but they are much too slow to provide the rotational energy reservoir for powering SNe through the MRM (Equation 12).

Various mechanisms have also been proposed for magnetic field amplification in collapsing cores with no or slow rotation, such as a convective dynamo (200), turbulent SASI motions in the postshock region (201), and exponential steepening of Alfvén waves created by fluid perturbations at Alfvén points in the accretion flow of the PNS (202). Moreover, Alfvén waves that are emitted

from the convective layer inside the PNS (and thereby extract energy from the rich reservoir of gravitational binding energy of the contracting remnant) have been suggested to provide extra energy to the stalled SN shock by dissipative heating (203), similar to the heating of the solar corona by Alfvén waves emerging from the surface of the Sun. Recent 2D core-collapse simulations with neutrino transport (114), however, find that these mechanisms are either inefficient or able to amplify the fields only locally. Large-scale fields with dynamical importance must reach magnetar strength (at least 10^{14}–10^{15} G), but in the absence of magnetorotational processes, they seem to require precollapse fields 100 times stronger than predicted by stellar evolution models.

Magnetic fields are therefore likely to play some role in all SN cores, but currently it seems that they are crucial for the explosion of only very rapidly spinning stars, which are probably linked to long GRBs and HNe (Section 2.3). MHD mechanisms have the advantage of not being strongly coupled to the mass in the gain layer and the mass-accretion rate through the stalled shock, which determine the explosion energy of SNe powered by neutrino heating (Equation 8). MHD-driven explosions can therefore be considerably more energetic than neutrino-driven SNe, where blast-wave energies of $\sim(1$–$2) \times 10^{51}$ erg may be the upper limit (Section 6.3). Large global deformation and well-collimated jets are expected to be generic to MHD explosions of very rapidly rotating stellar cores and seem to be characteristic of most hyperenergetic type Ib and Ic SNe.

Reliable and predictive multidimensional simulations of such phenomena are hampered by the fact that the true nature of MHD phenomena can be treated only in 3D, and such models should also include reasonably realistic neutrino transport. Another problem arises from the extreme dependence of the dynamical evolution on the initial conditions, in particular the rotation rate and profile of the stellar core (e.g., References 190–192) and the initial strength and geometry of the magnetic field (e.g., References 193 and references therein). Moreover, many MHD instabilities, among them the MRI, demand high numerical resolution, which both is particularly hard to achieve in 3D models and adds to the computational demands that result from long evolution times on the one hand and severe time-step constraints set by high Alfvén speeds, $v_A = B/\sqrt{4\pi\rho}$, on the other. The exploration of magnetorotational explosions will therefore remain a challenging task over the coming years.

4.5. Acoustic Mechanism

A new CCSN mechanism was envisioned (108, 109) on the basis of results of 2D hydrodynamic simulations, which did not yield explosions by neutrino-energy deposition. At late times after bounce ($\gtrsim 1$ s), large-amplitude dipole ($\ell = 1$) gravity-mode oscillations of the PNS core were excited by SASI sloshing motions of the postshock layer and by anisotropic accretion downdrafts. The PNS vibrations (with amplitudes of several kilometers) were damped when strong sound waves were sent into the surrounding medium. Running down the density gradient away from the PNS the waves steepened into secondary shocks. The dissipation of the latter helped to heat the postshock region. Thus, robust explosions were obtained for various progenitors. For the conversion rate of accretion power,

$$\dot{E}_{\text{acc}} = \frac{GM_{\text{NS}}\dot{M}}{R_{\text{NS}}} \sim 1.3 \times 10^{52} \, \frac{\text{erg}}{\text{s}} \left(\frac{M_{\text{NS}}}{1.5 \, M_\odot}\right) \left(\frac{\dot{M}}{0.1 \, M_\odot \, \text{s}^{-1}}\right) \left(\frac{30 \, \text{km}}{R_{\text{NS}}}\right), \qquad 15.$$

into acoustic power, one can estimate (108, 204)

$$\dot{E}_{\text{sound}} \sim \frac{\pi\rho}{2} \left(g_{\text{NS}} R_0\right)^{3/2} \, H_0^2 \sim 0.5 \times 10^{51} \, \frac{\text{erg}}{\text{s}} \, \rho_{11} \, g_{\text{NS},13}^{3/2} \left(\frac{R_0}{10 \, \text{km}}\right)^{3/2} \left(\frac{H_0}{3 \, \text{km}}\right)^2, \qquad 16.$$

(see also equation 1 of Reference 108). Here, R_0 is the accretion-stream radius, H_0 is the wave height, $\rho_{11} = \rho/(10^{11} \ \mathrm{g \ cm^{-3}})$ is the average density at the "surface" of the PNS core, and $g_{\mathrm{NS},13} = g_{\mathrm{NS}}/(10^{13} \ \mathrm{cm \ s^{-1}})$ is the average gravitational acceleration ($g_{\mathrm{NS}} = GM_{\mathrm{NS}}/R_{\mathrm{NS}}$) at the PNS surface. The reference value of $\dot{E}_{\mathrm{sound}}$ in Equation 16 is suggestive. This value exceeded the neutrino-energy deposition rate [$\sim \tau(L_{\nu_e} + L_{\bar{\nu}_e})$; Section 4.3.1] at late times in the numerical models. The violently vibrating PNS thus acted as a transducer by efficiently channeling accretion energy into sound.

The fraction of the accretion power that is converted into core g-mode activity of the PNS could not be extracted reliably from the numerical calculations of References 108 and 109, so the value of H_0 remains uncertain. Also, final numbers for the explosion energies could not be determined, but the 2D explosions occurred very late, which implies large NS masses and that the explosions tended to be low energetic. Fundamental questions about the excitation efficiency of the large-amplitude, low-order g-modes in the PNS remain to be answered; in particular, whether 3D simulations would also yield this phenomenon is unknown. So far, other groups have not been able to reproduce the results (e.g., Reference 106), perhaps because their models either were not evolved to sufficiently late times or had already exploded by neutrino heating.

A serious counterargument to the proposed scenario has been made (205). By employing perturbation analysis, the authors of this study concluded that nonlinear coupling between the low-order primary modes and pairs of high-order g-modes, whose small wavelengths cannot be resolved in hydrodynamical simulations, damps the low-order mode amplitudes to dynamically insignificant size. The thermalized pulsational energy is lost through neutrino emission.

4.6. Phase-Transition Mechanism

A first-order hadron-to-quark matter phase transition that occurs at a sufficiently low density can have dynamical consequences during the postbounce accretion phase of the collapsing stellar core. This discovery was made by Sagert et al. (206) and Fischer et al. (207), who used a hybrid EoS with a mixed phase that was softer than the hadronic phase and the pure quark phase. The quark phase was described by suitable choices of the parameters in the MIT bag model for strange (u, d, s) quark matter. In contrast to laboratory (heavy-ion collision) conditions, in which the proton fraction Y_p is close to 0.5, the mixed phase appeared at subnuclear densities for SN matter with $Y_p \lesssim 0.3$ and, for all proton-to-baryon ratios, showed a decrease of the transition density with higher temperatures. These results differ from those of other models for the hadron-quark phase transition; such models predict an increase of the phase-transition density with increasing temperature (e.g., References 208 and 209).

The very special properties of the hybrid EoS cause the PNS to become gravitationally unstable once it has accreted enough matter and has heated up during its contraction, thereby entering the transition to quark matter in a growing dense-core region. The decrease of the effective adiabatic index below the critical value for stability triggers a second, supersonic implosion to the denser pure quark phase, where the EoS suddenly stiffens again. The result is a considerable release of gravitational binding energy and the formation of a strong, second bounce shock, which catches up with the stalled primary shock to cause a SN explosion even in 1D models. When the second shock breaks out of the neutrinospheres, e^+ captures by neutrons in the shock-heated matter emit a $\bar{\nu}_e$ burst that may be detectable for a Galactic SN (210).

Although this is an interesting new scenario, the fine-tuning of the quantum chromodynamics phase transition is problematic. In particular, so far all the EoS versions that lead to explosions are not compatible with the (1.97 ± 0.04)-$M_\odot$ NS mass limit of PSR J1614-2230 (123). Changing the EoS parameters to reduce this inconsistency leads to a larger radius of the hybrid star and

a less extreme density difference between the hadronic and pure quark phases (207). Whether
SN explosions can be obtained with deconfinement scenarios compatible with PSR J1614-2230
remains to be determined.

5. OBSERVABLE SIGNALS FROM THE SUPERNOVA CORE

Neutrinos, GWs, and heavy-element formation in the neutrino-heated ejecta are direct probes of
the processes in the SN core. Because of the increase in sophistication of the models—especially in
terms of neutrino transport and the inclusion of relativistic effects (also in recent 2D simulations)—
and because of the growing understanding of hydrodynamic instabilities during the postbounce
accretion phase, interesting new aspects have been discovered and are poised to fundamentally
change our notion of some of the accompanying phenomena and implications of CCSNe.

5.1. Neutrinos

Neutrinos and antineutrinos of all flavors radiated from the SN core (**Table 1**) carry information
about the thermodynamic conditions (temperature, degeneracy) in the core, but they also reflect
dynamical processes associated with NS formation. A measurement of a neutrino signal from a
future Galactic event could thus help to unravel the explosion mechanism.

The shock-breakout burst of ν_e is a well-known example of such a dynamical feature. It emerges
when a flood of neutrinos freshly produced in shock-heated matter suddenly escapes when the
bounce shock reaches the neutrino-transparent regime at sufficiently low densities. Another (al-
beit more exotic) example is the neutrino flash connected to the hadron-quark phase transition
described in Section 4.6. Other instances include the pronounced rise of the mean energy of
heavy-lepton neutrinos (muon and tau neutrinos), ν_x, when a PNS approaches collapse to a BH
(211, 212) and possible—so far unclarified—signatures of magnetohydrodynamics.

Moreover, the large-amplitude radial oscillations (80) or low-multipole (dipolar, quadrupolar)
nonradial oscillations of the postshock layer (due to the SASI or due to convective activity for
higher-multipole asymmetries) lead to quasi-periodic variations of the accretion flow to the PNS
and to corresponding fluctuations of the accretion luminosity and mean energies of radiated
neutrinos (213). This effect is particularly strong for ν_e and $\bar{\nu}_e$, for which a significant part of the
luminosity [amounting to a fair fraction of the progenitor-specific accretion power (Equation 15)]
originates from $e^{\pm}$ captures on free nucleons in the hot accretion layer. In **Figure 7**, these fluctua-
tions are visible at $t \gtrsim 100$ ms after bounce. Note that the accretion luminosities depend strongly
on the progenitor, and in both the 11.2-$M_\odot$ and 15-$M_\odot$ explosion models, accretion continues
until the end of the simulated evolution, simultaneously with the accelerating expansion of the
shock (**Figure 6**) and with the development of positive ejecta energy. Ongoing accretion is obvious
because the ν_e and $\bar{\nu}_e$ luminosities are still considerably higher than those of ν_x, whereas after accre-
tion has ceased all luminosities become nearly equal (**Figure 5**) (106, 107, 159). The "luminosities"
in the left panels of **Figure 7** are energy-loss rates, $\dot{E}_\nu$, of the PNS ($\nu \in \{\nu_e, \bar{\nu}_e, \nu_\mu, \bar{\nu}_\mu, \nu_\tau, \bar{\nu}_\tau\}$), and
not observable fluxes; the variation amplitudes are therefore damped by the integration over all
directions.

The SASI and convective modulation of the neutrino emission was observed not only in 2D
simulations with RbR neutrino transport but also with multiangle treatment (see Section 3.2 for
a discussion of methods) (112). It may be detectable for a Galactic SN at a fiducial distance of
10 kpc with IceCube or future megaton-class instruments (214). The first 3D simulations with
approximate neutrino transport suggest that the variation amplitudes could be smaller than in
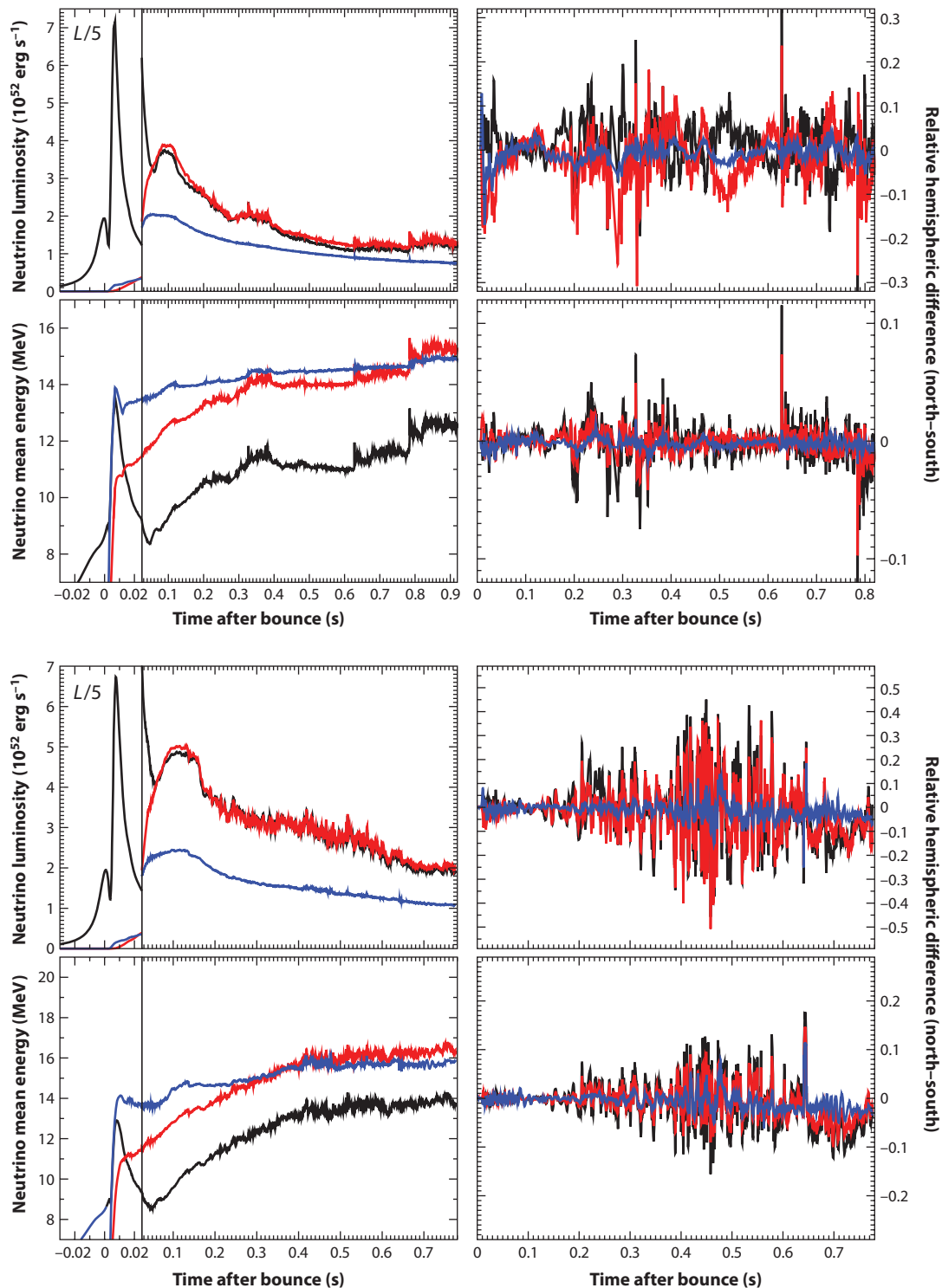
2D (96), but more and better 3D models with MG transport will be needed to obtain reliable information.

Another remarkable property of the neutrino signals in **Figures 5** and **7** is the close similarity and even crossing of the mean energies of $\bar{\nu}_e$ and ν_x (107, 213). Instead of the previous notion that ν_x are significantly more energetic than ν_e and $\bar{\nu}_e$—in other words, instead of a neutrino-energy hierarchy of $\langle \epsilon_{\nu_e} \rangle < \langle \epsilon_{\bar{\nu}_e} \rangle < \langle \epsilon_{\nu_x} \rangle$, typically with $\langle \epsilon_{\nu_x} \rangle \gtrsim 18-20$ MeV—state-of-the-art models now yield $\langle \epsilon_{\nu_e} \rangle < \langle \epsilon_{\bar{\nu}_e} \rangle \sim \langle \epsilon_{\nu_x} \rangle$ and $\langle \epsilon_{\nu_x} \rangle \lesssim 13-16$ MeV (**Figures 5, 7**) (213; also see Reference 79, where root-mean-square energies are given). The exact value depends on the time and EoS: A softer EoS leads to a more compact and hotter PNS and, therefore, higher mean energies (213).

Although during the later accretion phase the order of $\langle \epsilon_{\bar{\nu}_e} \rangle$ and $\langle \epsilon_{\nu_x} \rangle$ can be reversed (**Figure 7**), one obtains a mild hierarchy $\langle \epsilon_{\bar{\nu}_e} \rangle < \langle \epsilon_{\nu_x} \rangle$ during the PNS cooling phase (**Figure 5**). This hierarchy, however, diminishes to insignificant differences at very late times (seconds after bounce), when the mean energies of all neutrino kinds become nearly identical: $\langle \epsilon_{\nu_e} \rangle \approx \langle \epsilon_{\bar{\nu}_e} \rangle \approx \langle \epsilon_{\nu_x} \rangle$ (**Figure 5**) (107, 215). The late behavior can be understood by the flat temperature profile inside the PNS during the late cooling stage and the close proximity of the neutrinospheric positions of all neutrinos at that time. This proximity is caused by the strong dominance of neutral-current scatterings in the effective opacity (i.e., inverse mean free path) for thermal coupling between neutrinos and stellar medium, $\kappa_{\mathrm{eff}} \equiv \sqrt{\kappa_e(\kappa_s + \kappa_e)}$ (where κ_e and κ_s are the opacities for neutrino-production processes and nucleon scatterings, respectively), at conditions wherein e^- are strongly degenerate and neutrons start to become degenerate (215).[4] The close similarity between $\langle \epsilon_{\nu_x} \rangle$ and $\langle \epsilon_{\bar{\nu}_e} \rangle$ during the early postbounce and accretion phases is fostered by nucleon-nucleon bremsstrahlung as the main ν_x production channel (219) because it shifts the energy sphere of ν_x to a lower temperature (220). However, the effect is considerably enhanced (compare the two cases discussed in Reference 107) by the energy losses of ν_x in collisions with free nucleons $N = n, p$ (inelastic— or, better, nonconservative—nucleon recoil) (**Table 1**). Such losses occur when the neutrinos diffuse out through the (optically) thick scattering layer between the energy and transport spheres (220, 221). The small but very frequent energy transfers, with an average value per collision of $\langle \Delta \epsilon_\nu \rangle_{\nu N} \sim \epsilon_\nu (6 \, k_B T - \epsilon_\nu)/(m_N c^2)$ (222), can force the ν_x spectrum to become even softer than that of $\bar{\nu}_e$, whose production in a hot accretion layer by e^+ captures on neutrons is very efficient.

The close similarity between the spectra of all the neutrinos and the corresponding relevance of the nonconservative nucleon recoils, which is still widely ignored, affect (*a*) the consequences of neutrino-flavor conversions, such as the rise time of the detectable $\bar{\nu}_e$ signal (223), and (*b*) neutrino-induced or flavor oscillation–dependent r-process nucleosynthesis in SNe (224, 225). Also, the steep rise of $\langle \epsilon_{\nu_x} \rangle$ before BH formation, which was found without nonconservative nucleon recoils being taken into account (211, 212), may be affected.

←――

Figure 7

Neutrino signals from general relativistic two-dimensional simulations of core collapse and explosion of the 11.2-$M_\odot$ (*top*) and 15-$M_\odot$ (*bottom*) stars shown in **Figure 6** (146). (*Left*) The luminosities, namely the total neutrino-energy loss rates of the proto–neutron star (PNS) (*upper panels*), and the mean energies, defined by the ratio of total neutrino energy-loss rate to number-loss rate, $\dot{E}_\nu/\dot{N}_\nu$ (*lower panels*). Black lines represent ν_e; red represents $\bar{\nu}_e$; and blue represents one kind of heavy-lepton neutrino, ν_x. (*Right*) The corresponding relative hemispheric differences after core bounce (the infall remains spherical). All these quantities were measured in the lab frame at a large distance. Note that the fluctuations, sudden jumps, and north-south differences at $t > 300$ ms in the upper plot are caused by violent, time-dependent, anisotropic downflows and by corresponding changes of the accretion rate of the PNS.

――――――――――――――――――――――――

[4]For the influence of the EoS-specific nucleon potential energies in dense NS matter, which affect the β processes of ν_e and $\bar{\nu}_e$ but were ignored in the models in **Figures 5** and **7**, see References 216–218.

5.2. Gravitational Waves

Any nonspherical, accelerated mass motions in the SN core act as a source of GWs, whose amplitude at a source distance D scales with the second derivative of the mass-quadruple moment: $h \sim (2G/c^4)(\ddot{Q}/D)$. The GW signal reflects the activity phases that are also partly visible in the neutrino-luminosity variations (compare **Figures 7** and **8**). Convective overturn caused by negative entropy gradients in the deceleration region of the bounce shock and in the neutrino-heating layer, the violent SASI sloshing of the whole postshock volume, and the impact of accretion downdrafts (which occur even after the onset of the explosion) induce surface g-modes in the outer layers of the PNS (213), whose frequency determines that of the GW emission (226). Because the
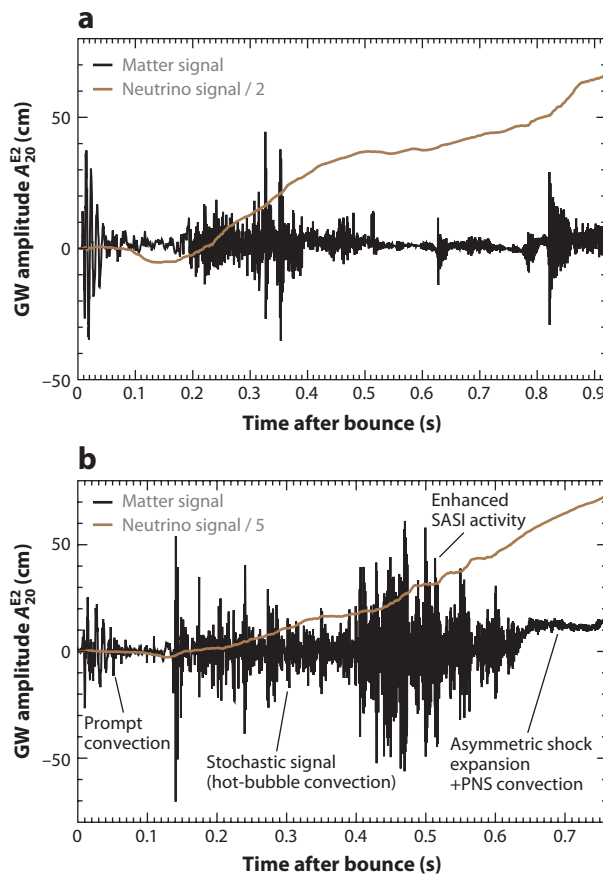
Figure 8

Amplitudes of gravitational waves (GWs) from the general relativistic two-dimensional simulations of core collapse and explosion of (*a*) the 11.2-$M_\odot$ star and (*b*) the 15-$M_\odot$ star shown in **Figure 6** (146). The light brown lines (scaled down by factors of two and five in panels *a* and *b*, respectively) represent the growing amplitude connected with the asymmetric neutrino emission. The matter signal (*solid black line*) exhibits activity phases associated with strong, prompt postbounce convection (for $t_{pb} \lesssim 50$ ms), increasingly violent convective and standing accretion shock instability (SASI) mass motions in the postshock layer before the explosion sets in [between ~100 ms and 350 ms (500 ms) in the 11.2-$M_\odot$ (15-$M_\odot$) case], and the continued impact of asymmetric accretion downdrafts on the proto–neutron star (PNS) after the launch of the explosion. The nonzero value of the matter signal at late times is a consequence of the aspherical expansion of the shocked ejecta.

buoyancy (Brunt–Väisälä) frequency connected to the gravity waves depends on the compactness of the PNS (see the text following Equation 3), both the stiffness of the EoS (213) and GR gravity are crucial to predict the GW spectrum. For relativistic models, the spectrum peaks around 800 to 1,000 Hz, whereas Newtonian simulations yield significantly lower frequencies (146).

GWs are expected to carry characteristic signatures of the explosion mechanism. Whereas wave components associated with long-lasting convective and SASI activity and a broadband signal seem typical of neutrino-driven explosions, the large-amplitude g-mode oscillations of the PNS core, which are essential for the acoustic mechanism, would lead to a dramatic rise of the GW amplitude shortly before the blast sets in (227). In contrast, rapid stellar core rotation, as required for MHD explosions, would produce a powerful GW burst at core bounce, which could be followed by postbounce emission due to triaxial instabilities (18).

The GW features and activity phases observed in 2D models are also found in 3D simulations, although the amplitudes may be different. Without symmetry constraints, however, the detailed signal structure varies strongly with the observer direction and does not take a standard form (93, 96, 228, 229).

5.3. Heavy Elements

In addition to reprocessing shock-heated stellar layers by explosive burning, nucleosynthesis takes place in the neutrino-heated ejecta in the close vicinity of the NS. The neutrino-heated ejecta consist of two components and have great potential for diagnostics of the SN mechanism.

The first component consists of early ejecta from the phase of shock revival. Its composition at freeze-out depends on the expansion timescale, which is intrinsically linked to the blast dynamics and thus to the explosion mechanism, but it also depends on the neutron-to-proton ratio set by the competition of $e^{\pm}$ captures on nucleons and the inverse ν_e and $\bar{\nu}_e$ captures (the top two β processes in **Table 1**).

A good example of the relevance of these effects is supplied by recent 2D results of O-Ne-Mg-core explosions, in which acceleration by convective buoyancy expels early ejecta so rapidly that this material retains a neutron excess sufficient for weak r-processing; in contrast, in 1D models β reactions in the more slowly ejected plasma lift Y_e close to 0.5 and above (33). It will be interesting to explore the combination of composition and asymmetry differences of the early ejecta in magnetorotational explosions compared with neutrino-driven ones as soon as self-consistent, well-resolved multidimensional MHD models with sophisticated neutrino transport (instead of no or highly simplified neutrino treatment) become available.

The second component is the neutrino-driven wind blown off the surface of the hot PNS by neutrino-energy deposition above the neutrinosphere after the explosion has been launched. The properties of this essentially spherically symmetric outflow—in the absence of rotation and/or strong magnetic fields—depend on the strong gravity field of the NS and on the properties (luminosities and spectra) of the radiated neutrinos, which determine the strength of the heating (230, 231). Again, the β processes of free nucleons (**Table 1**) set the neutron-to-proton ratio of this environment. For sufficiently high entropy and sufficiently large neutron excess, this wind may provide an interesting site for r-process nucleosynthesis (232).

However, in addition to the long-standing problem of insufficient entropy (233, 234), sophisticated hydrodynamic models find the wind to be proton rich (107, 159). This quality is a consequence of the close similarity between the spectra and luminosities of ν_e and $\bar{\nu}_e$ during the PNS cooling phase, $L_{\bar{\nu}_e} \approx L_{\nu_e}$ and $\langle \epsilon_{\bar{\nu}_e} \rangle \approx \langle \epsilon_{\nu_e} \rangle$ (Section 5.1) (**Figure 5**), which enforces $Y_e > 0.5$. Because (230)

$$Y_e \sim \left[1 + \frac{L_{\bar{\nu}_e}(\varepsilon_{\bar{\nu}_e} - 2\Delta)}{L_{\nu_e}(\varepsilon_{\nu_e} + 2\Delta)} \right]^{-1}, \qquad\qquad 17.$$

where $\varepsilon_\nu = \langle \epsilon_\nu^2 \rangle / \langle \epsilon_\nu \rangle$ and $\Delta = (m_n - m_p)c^2 \approx 1.29$ MeV, values of $Y_e < 0.5$ require considerably more energetic $\bar{\nu}_e$ than ν_e, satisfying $\varepsilon_{\bar{\nu}_e} - \varepsilon_{\nu_e} > 4\Delta$. Recent studies showed that the nucleon potential energies in dense NS matter, connected to the nuclear symmetry energy, may cause sufficiently large differences of ν_e and $\bar{\nu}_e$ spectra to bring the wind Y_e slightly below 0.5 (216–218); it remains to be seen whether this reduction allows for an r-process.

A dominance of protons prevents r-processing but might enable a νp process (235, 236). Active-sterile $\nu_e - \nu_s$ conversions involving a possible sterile neutrino ν_s in the eV mass range, as suggested by an anomaly of reactor $\bar{\nu}_e$ spectra and their distance and energy variation, can decrease the proton excess by removing ν_e and thereby suppressing their absorption on neutrons. A recent investigation based on an ECSN model, however, revealed only a modest effect that was insufficient for an r-process (237). However, the results depend in a complex way on the interplay between $\nu_e - \nu_s$ MSW matter oscillations and collective $\nu\bar{\nu}$ flavor conversion, which strongly reduces the pure matter effect. More exploration seems necessary.

6. EXPLOSION PROPERTIES AND COMPACT REMNANTS

The explosion mechanism establishes the link between progenitor stars and SNe and their remnants. It is therefore natural to seek observables that might provide indirect evidence of the processes that trigger the onset of the blast. In the following subsections, we briefly discuss the implications and limitations of neutrino-driven explosions with respect to pulsar kicks, SN asymmetries, and progenitor-dependent explosion and remnant properties.

6.1. Pulsar Kicks and Spins

Young pulsars possess average space velocities of approximately 400 km s^{-1}; some of them are even faster than 1,000 km s^{-1} (240). This velocity is too high to be understood by the breakup of binary systems in SN explosions, and natal kicks of the NSs are required (241).

An asymmetric initiation of the explosion can naturally impart a recoil velocity to the NS due to linear momentum conservation. Impulsive momentum transfer by hydrodynamic forces of anisotropically expelled gas during the convective launch phase of the explosion, however, can hardly account for more than $\sim$200 km s^{-1}, even in the most optimistic case (242). Therefore, a strong unipolar asymmetry in the progenitor star prior to collapse—in contrast to the higher-multipole asymmetries that usually result from the stochastic and chaotic growth of hydrodynamical instabilities seeded by small, random perturbations (Section 4.3.3)—has been hypothesized to define a preferred direction in which the SN blast could break out with the highest velocities (243, 244). However, stellar evolution models (self-consistently evolved in 3D through all advanced burning stages up to gravitational instability) that could lend convincing support to the existence of such global, low-multipole precollapse asymmetries do not yet exist.

Anisotropic neutrino emission is another potential NS kick mechanism by which the NS could achieve a recoil velocity of $v_{NS} \sim \xi_\nu (33,000 \text{ km s}^{-1})(E_\nu/3 \times 10^{53} \text{ erg})(M_{NS}/1.5 \ M_\odot)^{-1}$. An asymmetry ξ_ν of 1% of the total neutrino energy loss would thus kick the NS to more than 300 km s^{-1}. The asymmetric neutrino emission associated both with postbounce accretion (94, 95) and with the convective activity during the PNS cooling evolution (156), however, is highly time variable and nonstationary in space and time; therefore, it can hardly account for recoil velocities of more than 10 km s^{-1}. Exotic mechanisms that invoke ultrastrong NS magnetic dipole fields and nonstandard, as-yet-uncertain neutrino properties have therefore been suggested as speculative solutions (e.g., Reference 245 and references therein).

On the basis of 2D explosion simulations by Scheck et al. (94, 246), whose results received recent confirmation by 2D (247, 248) and 3D models (95; A. Wongwathanarat, H.T. Janka & E.
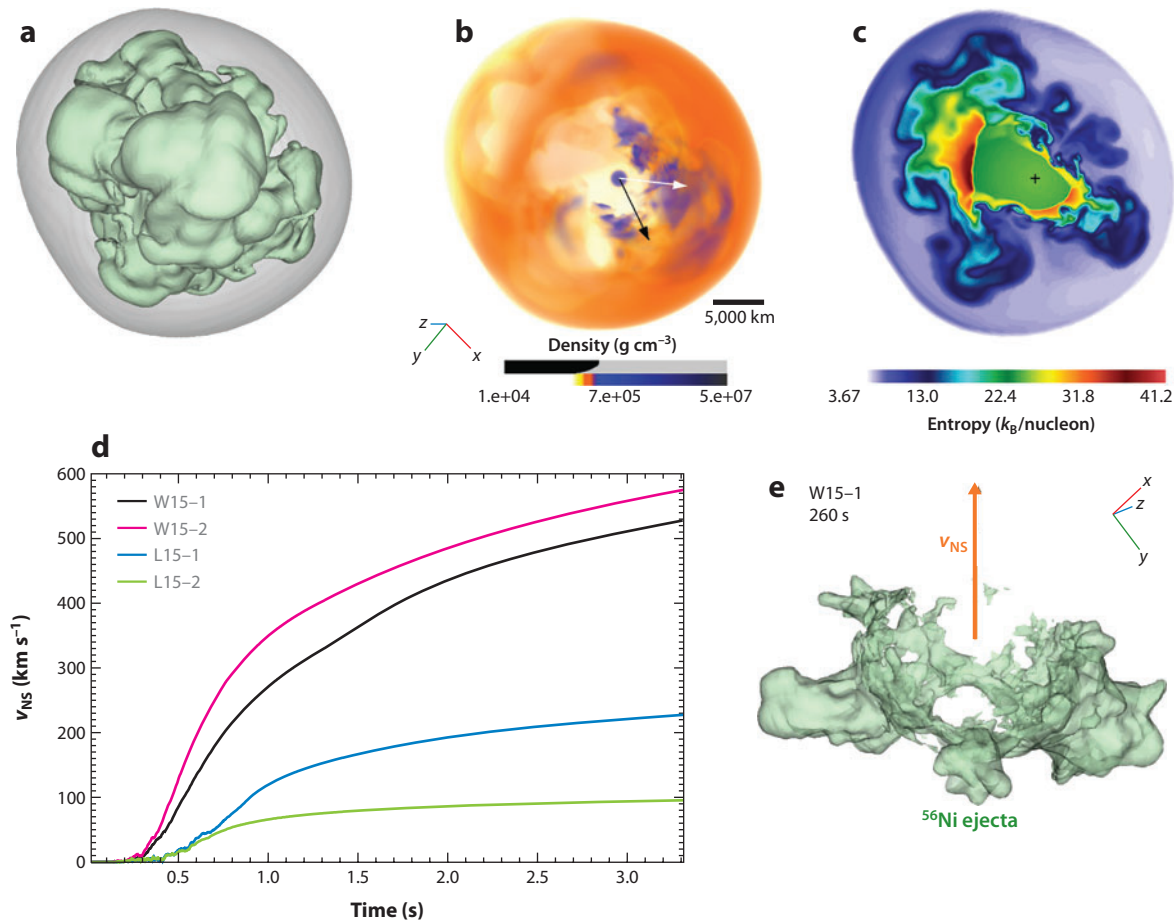
Figure 9

Neutron star (NS) kicks and anisotropic Ni ejection for asymmetric supernova (SN) explosions in three-dimensional (3D) simulations (95; A. Wongwathanarat, H.T. Janka & E. Müller, manuscript in preparation). (*a–c*) Entropy isosurfaces of SN shock and convective bubbles (*a*) and ray-casting image of the density (*b*) at $t = 1.3$ s after bounce. The deformed boundary is the shock; the viewing direction is normal to the plane of NS kick and spin vectors (*white and black arrows*), which define the plane of the entropy distribution (*c*). The NS (*black cross*) is clearly displaced from the geometrical center of the expanding shock toward the side of weaker explosion. It is accelerated mainly by the asymmetric gravitational attraction of slower-expanding, dense ejecta clumps (*intense red and blue, panel* b) (*d*) Recoil velocity of the NS versus time for four 3D explosion simulations of different stars. The acceleration continues even later than 3 s, and kicks of >600 km s^{-1} are reached. (*e*) Anisotropic production of radioactive ^{56}Ni by explosive nuclear burning behind the expanding shock. For large NS kicks, Ni is ejected preferentially in the direction where the shock is stronger, that is, opposite to the NS motion (*red arrow*).

Müller, manuscript in preparation), what is probably the most plausible origin of the NS velocities was proposed. Scheck et al. showed not only that the asymmetric expulsion of gas exerts "contact forces" during the few hundred milliseconds in which the explosion is launched and the ejecta and PNS interact hydrodynamically, but that the asymmetric ejecta exert a long-lasting, anisotropic gravitational pull, which can accelerate the PNS over seconds to velocities of many hundreds of kilometers per second (**Figure 9**). For particularly large asphericity of the ejecta, an NS velocity of $v_{NS} > 1,000$ km s^{-1} was obtained (94). A hemispheric asymmetry with a mass distribution of only $\Delta m = \pm 10^{-3}$ $M_{\odot}$, in a shell expanding away from the NS from an initial radius $r_i = 100$ km

with $v_s = 3,000$ km s^{-1}, can tug the NS to a velocity of $v_{NS} \approx 2G\Delta m/(r_i v_s) \approx 900$ km s^{-1} (95; A. Wongwathanarat, H.T. Janka & E. Müller, manuscript in preparation).

Gravitational forces of anisotropically ejected gas can thus mediate an efficient, long-lasting acceleration of the NS by transferring momentum from the anisotropically ejected matter to the compact remnant. Because the NS is gravitationally pulled by the slower, usually denser ejecta associated with a weaker explosion shock, Wongwathanarat et al. (A. Wongwathanarat, H.T. Janka & E. Müller, manuscript in preparation) expect the bulk of the Fe-group nuclei and of other elements heavier than ^{28}Si, which are explosively produced in the shock-heated ejecta, to be expelled preferentially in the direction opposite that of the NS motion. These authors predict a very strong asymmetry of the Ni ejection in the case of large NS kicks (**Figure 9**), which could be an observationally accessible, characteristic feature of the hydrodynamical-gravitational kick mechanism.

Asymmetrical convective downdrafts and rising bubbles, as well as violent, low-multipole SASI sloshing modes, which have spiral components in 3D, can establish angular momentum separation between PNS and ejecta and thus may cause considerable PNS rotation even if the stellar core did not rotate before collapse (82, 83) [because of the use of an inner boundary condition, however, these results have been questioned (249)]. Naturally, any anisotropic mass infall that hits the accretor not exactly head-on can exert a torque and spin up the PNS. A mass $\Delta m = 10^{-3}$ $M_\odot$ that has an impact velocity $v_{imp} \sim \sqrt{2GM_{NS}/R_{NS}} \sim 10^{10}$ cm s^{-1} and an impact parameter $d \equiv \zeta R_{NS} \sim$ 30 km when colliding with the NS transfers an angular momentum of $\Delta J_{NS} = \Delta m \ v_{imp} d \sim$ 6×10^{46} g cm^2 s^{-1}, which corresponds to a NS spin period of $T_{NS} = 2\pi I_{NS}/\Delta J_{NS} \sim 0.2$ s for a typical value of the NS moment of inertia of $I_{NS} \sim 2 \times 10^{45}$ g cm^2. Indeed, 3D explosion simulations yield T_{NS} in the range of hundreds of milliseconds to seconds (95; A. Wongwathanarat, H.T. Janka & E. Müller, manuscript in preparation). Nevertheless, angular momentum transferred to the PNS by hydrodynamical flows during the development of the explosion and in the postexplosion accretion phase is unlikely to be sufficient to account for the estimated NS birth spin periods of order $\sim$10 ms, which seems to require rotation of the collapsing stellar core (36, 250). Explaining a possible spin-kick correlation of observed NSs remains a challenge for any kick mechanism connected to explosion asymmetries of progenitor stars with or without rotation.

6.2. Supernova Asymmetries

The large asymmetries imprinted on the ejecta by the violent, nonradial mass motions in the SN core, which precede and accompany the neutrino-driven revival of the blast wave, seed the growth of secondary Rayleigh–Taylor instability in the shock-accelerated outer shells of the exploding star (251). Because the developing Rayleigh–Taylor mushrooms are denser than the surrounding gas, they are less decelerated than their environment and can penetrate the composition interfaces of the progenitor, retaining high velocities as the SN ejecta expand. Thus, they carry freshly synthesized radioactive Ni and other heavy elements from the vicinity of the nascent NS into the outer stellar layers. Significant amounts of the initially innermost ejecta can be mixed deep into the He shell, and even the H layer, of the disrupted star (252), thereby destroying the well-stratified onion-shell structure of the progenitor.

In 3D simulations of a SN 1987A progenitor model, large Ni-dominated clumps (containing up to several 10^{-3} $M_\odot$ of ^{56}Ni) sped through the stellar H envelope at up to 4,500 km s^{-1} (**Figure 10**) (238). This finding could explain the mixing phenomena and asymmetries observed in SN 1987A, such as the detection of X-rays and γ-rays from the radioactive Ni decay that occurred much earlier than predicted by 1D explosion models (69). The outward mixing of radioactive Ni and the inward displacement of H can account for the shape and width of the light-curve maximum of SN 1987A (V. Utrobin, private communication).
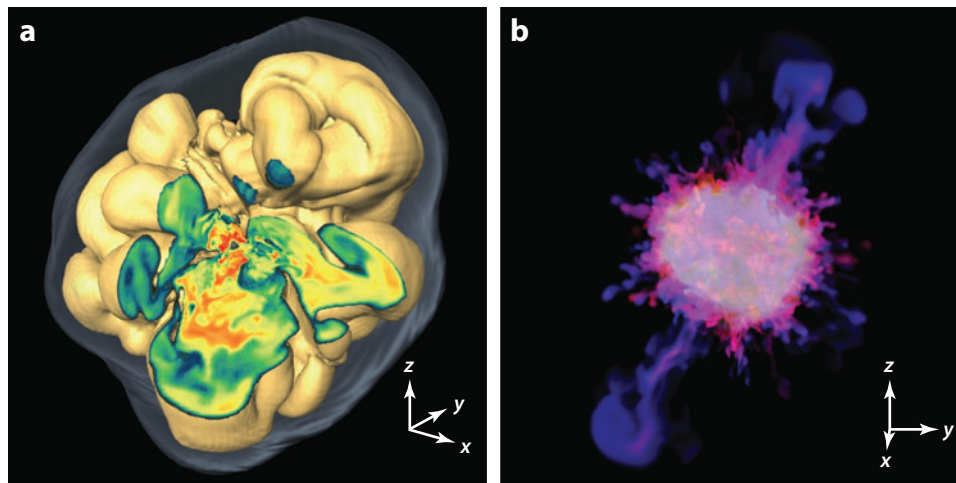
Figure 10

(*a*) Asymmetric shock front (*outer bluish surface*) and mushroom-like, high-entropy bubbles of neutrino-heated plasma around the central NS (*dark gray surface near the middle*) at 0.5 s after bounce in a three-dimensional SN simulation (238). The shock front has a diameter of ~4,000 km. An octant is cut out to show the entropy distribution (color coded between ~10 and 21 k_B per nucleon from blue to yellow to red) in the expanding Rayleigh–Taylor mushrooms surrounded by cooler accretion downdrafts. All visible structures have grown from tiny, random seed perturbations by hydrodynamic instabilities. (*b*) Asymmetric ejection of different chemical elements during the explosion in panel *a*, but ~9,000 s later in the supernova (SN) evolution (238). The side length of the displayed volume is approximately 7.5×10^7 km. The largest bubbles in panel *a* have seeded the growth of the most prominent Rayleigh–Taylor fingers in the right picture, which expand at up to 4,500 km s^{-1}. They are surrounded by the helium and hydrogen of the outer stellar shells (not visible). Together with the smaller features, they carry heavier chemical elements from deep stellar layers far into more slowly expanding, lighter SN material. Blue filaments contain dominantly nickel, red fingers contain mostly oxygen, and green is associated with carbon. A mix of nickel and oxygen appears in pink. The whitish glow results from a contamination with other colors as a consequence of the volume rendering for the visualization.

However, it is still unclear whether explosion asymmetries associated with the development of hydrodynamic instabilities in the SN core and the subsequent growth of mixing instabilities in the stellar envelope can explain the prolate shape of the SN 1987A ejecta cloud. Also, it remains to be seen whether they can account for the extremely fast "jet" structures observed ahead of the explosion shock in the Cassiopeia A SN remnant. Moreover, the global asphericity of most very energetic type Ib/c SNe might require larger nonradial deformation than the asymmetric structures that can stochastically grow from initially small random perturbations.

6.3. Neutron Stars and Black Holes

Remnant masses and explosion properties (e.g., energy, ejected ^{56}Ni mass) and their systematics with the progenitor mass also carry information about the explosion mechanism. The observational foundation of determined or constrained NS and BH masses (124, 253, 254), SN-progenitor connections (26, 27), and estimated explosion parameters (**Figure 3**) (e.g., References 24 and 25) is becoming increasingly strong.

The observed mass distribution of compact remnants and its possible gap between ~2 and 5 $M_\odot$ at the boundary between NSs and BHs led some scientists to infer that the SN engine must launch the (neutrino-powered) explosion within 100 to 200 ms of bounce in order not to overproduce

remnants in the gap (255, 256). This inference was considered an argument that the mechanism is supported by Rayleigh–Taylor (convective) rather than SASI instability. However, in the SN core both of these nonradial instabilities occur simultaneously (76, 160) and cannot be separated simply on the basis of a timescale argument. Moreover, the population evolution models from References 255 and 256 used very simple theoretical considerations to determine the explosion energy for early and late explosions and to estimate the fallback mass of matter that initially moves outward but ultimately fails to escape because of insufficient blast-wave energy. The analytic theory ignores, for example, dynamical effects and the nonnegligible additional power carried by the early neutrino-driven wind (94). Other approaches to predicting the mass distributions of NSs and/or BHs were based either on piston-driven explosions with predefined mass cut and explosion energy (e.g., Reference 257) or on a single-parameter criterion to distinguish progenitors that are likely to explode or not (258).

In Reference 239, an alternative approach was adopted. Hydrodynamical simulations in 1D were performed for a large set (roughly 100) of the solar-metallicity progenitors of Reference 22 by use of an analytic, time-dependent two-zone model of the cooling, contracting PNS, whose free parameters were calibrated such that the explosion energy and ^{56}Ni mass of SN 1987A were reproduced for stars with a zero-age main-sequence mass of around 20 $M_\odot$. The effects of accretion luminosity were taken into account through simplified neutrino transport (94). With this prescription, all stellar collapses and possible explosions were simulated for at least 15 s beyond core bounce and were followed after the PNS cooling for hours to days until the fallback mass was determined.

Results of the calculations (**Figure 11**) reveal many interesting insights that, of course, depend on the considered progenitor set:

1. Because the stellar structure varies nonmonotonically, the SN properties depend on the progenitor mass in a complex way. Large differences of the explosion characteristics are possible for small mass differences.
2. Failed explosions with BH formation seem possible for progenitors below 20 $M_\odot$, and successful SNe with NS formation are also found between 20 and 40 $M_\odot$.
3. Neutrino-driven explosions with energies in excess of 2×10^{51} erg and ^{56}Ni production of significantly more than $\sim$0.1 $M_\odot$ seem unlikely.
4. The time of the onset of the SN blast (measured by the moment the shock passes 500 km) varies between $\sim$0.1 and 1.1 s, so it includes early and late cases. Later explosions tend to be less energetic because less mass is available for heating by neutrinos.
5. The NS baryonic masses are in the range between $\sim$1.2 and 2 $M_\odot$. The smallest BH, formed by fallback, contains 6.5 $M_\odot$; all the other BHs originate from failed explosions and contain all the mass of the progenitor at collapse (>8.5 $M_\odot$). The possible gap of the observed remnant distribution is clearly reproduced.
6. Fallback is larger for the lower-mass progenitors, wherein an extended H envelope leads to a stronger reverse shock. The result of the little fallback in solar-metallicity progenitors is compatible with conclusions based on an analysis of observed double-NS systems (259).
7. Although the remnant mass is an almost monotonic function of the enclosed mass at the base of the O-burning shell, the latter mass is no reliable indicator for the fate of the star because some models with relatively small Si cores do not explode.
8. Neutrino-driven explosions are fostered by large jumps in the stellar density and entropy profiles (**Figure 2**), reducing the mass-infall rate (and ram pressure) and allowing the shock to expand (Equation 2).

Certainly, these results are based on 1D simulations, and many approximations were made. Therefore, they can be only a very first step; nevertheless, they are enlightening concerning
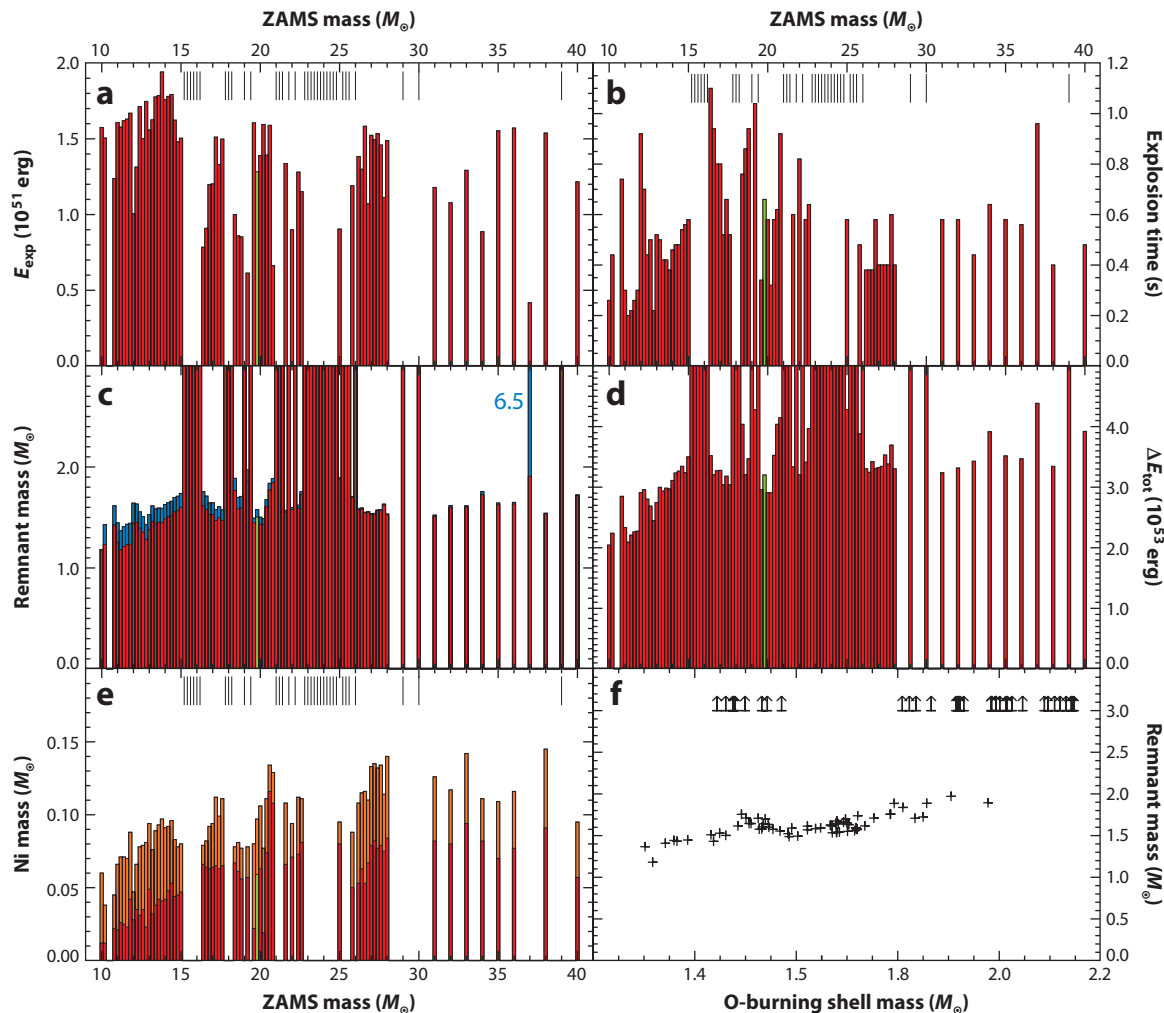
Figure 11

Explosion and remnant properties predicted by parameterized one-dimensional neutrino-driven supernova (SN) simulations (239) of a large set of progenitor stars (22). (*a*) Explosion energy, (*b*) time of onset, (*c*) baryonic remnant mass, (*d*) neutrino-energy release by the compact remnant, and (*e*) ejected Ni mass are shown as functions of stellar birth [zero-age main-sequence (ZAMS)] mass. (*f*) The compact remnant mass versus the enclosed mass at the bottom of the O-burning shell of the progenitor. Neutrino cooling of the dense neutron star core was prescribed such that the properties of SN 1987A were roughly reproduced for ∼20 $M_\odot$ stars (*green histogram bar*). Accretion neutrino luminosity was self-consistently computed by approximate neutrino transport. The ticks in some panels mark masses for which the computed models did not explode. Bars of remnant masses reaching to the upper panel edge (3 $M_\odot$) and arrows in panel *f* signal the formation of a black hole (BH) containing the whole mass of the star at collapse. The only exception is the 37-$M_\odot$ progenitor, where the explosion ejects ∼3.2 $M_\odot$ while fallback creates a BH with 6.5 $M_\odot$. Blue segments indicate fallback masses, and orange segments represent Ni-mass uncertainties due to unclear Ni abundance in the *ν*-heated ejecta.

the implications of neutrino-powered explosions. These results challenge numerous paradigms for the progenitor-explosion and progenitor-remnant connections. In particular, the limited blast-wave energy and Ni production support arguments in favor of another explosion mechanism for HNe. These events are likely to be triggered by magnetorotational processes. More research, observational and theoretical, will be required to clarify whether there is a continuous transition

between the two, associated with a varied degree of progenitor rotation and leading to a continuous spectrum of explosion energies that reach from the neutrino-powered regime of $E_{exp} \lesssim 2 \times 10^{51}$ erg to the hyperenergetic regime of $E_{exp} > 10^{52}$ erg, as has been suggested by some phenomenological studies (**Figure 3**).

7. SUMMARY, CONCLUSIONS, AND OUTLOOK

SN theory has made remarkable progress over the past decade, advanced by the common interests of the astrophysics, particle (neutrino) physics, nuclear physics, and gravitational physics communities and by an increasing number of active (young) researchers in the field. A deeper understanding of the physical mechanisms that initiate and fuel SN and HN explosions of massive stars is crucially important not only for establishing the progenitor-remnant connection but also for predicting the properties of stellar explosions, their nucleosynthetic output, and the characteristics of their GW and neutrino signals.

The most sophisticated current simulations demonstrate that neutrino-energy deposition can power ECSNe (even in spherical models) of ~ 9-$M_\odot$ stars with O-Ne-Mg-cores near the lower mass limit for SN progenitors (**Figure 5**). Overall, the features of such explosions, namely low energy and little Ni production, seem to be compatible with observational candidates such as the Crab SN and some faint transients. Multidimensional simulations suggest these explosions to be potential sources of light r-process nuclei up to Ag and palladium (Section 5.3). Several groups have also reported successful neutrino-driven explosions (with MG neutrino transport) for Fe-core progenitors above 10 $M_\odot$ (Section 4.3.2) (**Figures 4** and **5**). Definitive confirmation of the viability of this mechanism for a wider range of progenitor masses therefore seems to be within reach.

The onset of the explosion can be understood as a global runaway instability of the accretion layer, whose initiation depends on the power of neutrino-energy deposition. Although the exact mode of the runaway is still a matter of exploration and debate (e.g., Is it low-multipole SASI or higher-multipole convective? Is it oscillatory or nonoscillatory?), its threshold in terms of the driving neutrino luminosity is lowered by nonradial fluid motions in the neutrino-heating layer. Such flows play a supportive role because they stretch the residence time of matter in the gain region and therefore decrease the heating timescale and increase the efficiency of neutrino-energy deposition, which leads to successful explosions even when sophisticated spherical models fail (Section 4.3.3). The efficiency of neutrino-energy transfer, the growth conditions and growth rates of different hydrodynamic instabilities, and the critical luminosity threshold for an explosion may depend on the dimension and thus ultimately require simulations in 3D; they also depend on putative details of the physics ingredients, such as approximations for the energy and velocity dependence of the neutrino transport, the neutrino-interaction rates, GR, and the contraction of the nascent NS in response to the nuclear EoS (Section 3) (**Figure 4**). Moreover, the outcome of the complex neutrino-hydrodynamical simulations can be sensitive to the numerical resolution, which naturally is subject to limitations in full-scale, multidimensional SN-core models.

While detailed modeling of the processes in collapsing stars is pushing forward from the second dimension to the third, which poses considerable computational challenges and demands mainly for the neutrino transport, studies are increasingly beginning to explore the observational consequences of neutrino-driven explosions. In view of existing and upcoming big detection facilities, neutrino and GW signals (**Figures 5**, **7**, and **8**) are especially relevant for SN-core diagnostics targeting a future galactic SN. Neutrino signals could even yield valuable information about the particle properties of the neutrinos, provided that the characteristics of the SN emission are sufficiently well understood (e.g., References 223, 260, 261, and 262). Sophisticated neutrino transport and interaction treatments have revealed interesting signal features, such as an amazing

robustness of the neutronization ν_e burst (260), characteristic differences of the rise time of the $\bar{\nu}_e$ and ν_x emission after bounce (223), luminosity variations associated with nonsteady flows in the accretion layer (112, 213), and a close similarity between the luminosities and spectra of neutrinos and those of antineutrinos of all flavors during the PNS cooling phase (Section 5.1) (**Figure 5**) (107, 215); these features have important consequences for SN nucleosynthesis (Section 5.3).

Although a galactic SN in the near future is a realistic possibility, it will be a unique event and may not provide evidence of wider validity. Photometric and spectroscopic diagnostics of extragalactic SNe and of gaseous, young SN remnants, which reveal information about explosion energies, ^{56}Ni production, ejecta masses, asymmetries, and composition, as well as progenitor constraints (**Figure 3**), are therefore extremely valuable, and more diagnostics will be desirable. First-principle explosion models are becoming mature enough to be linked to such observations, a possibility that suggests a new area for future research. Neutrino-driven explosion models are also beginning to allow for predictions of compact remnant masses (NSs and BHs), kicks, and spins.

Nonradial hydrodynamic instabilities in the collapsing stellar core, which can grow from small, random initial perturbations before neutrino heating revives the stalled shock, cause low-multipole asymmetries that trigger anisotropic and inhomogeneous expulsion of matter. Hydrodynamic instabilities in the SN core therefore do not only yield a natural explanation of the origin of pulsar kicks up to more than 1,000 km s^{-1} (Section 6.1) (**Figure 9**); they also seed large-scale mixing processes in the exploding star, thereby accounting for the penetration of high-velocity clumps of inner-core material into the H and He ejecta of well-observed SN explosions (Section 6.2) (**Figure 10**).

Early results from a systematic exploration of the progenitor-SN connection based on the neutrino-heating mechanism show that the explosion properties are strongly sensitive to the stellar structure. They also show, for the set of stellar models that were utilized (22), large variations even within narrow progenitor-mass intervals (Section 6.3) (**Figure 11**). These explosion models can reproduce the fundamental properties of the empirical remnant-mass distribution, but they reveal that neutrino-driven explosions are unlikely to explain SN energies above $\sim 2 \times 10^{51}$ erg and Ni masses significantly higher than 0.1 $M_\odot$. These findings highlight the need for an alternative engine that can power stellar blast waves with energies from several 10^{51} erg up to more than 10^{52} erg. Such hyperenergetic events, which typically also exhibit unusually large Ni ejection (**Figure 3**) and deformation, are probably energized by magnetorotational effects.

Many questions remain to be answered in this context and require more observations and theoretical work. What discriminates the progenitors of "normal" SNe from those of HNe? Is rapid rotation of the progenitors the crucial parameter? Is it connected to binary evolution? Is there a continuous spectrum of stellar explosions that connect the SN and HN regimes? Is a mixed mechanism—neutrino heating in combination with magnetorotational energy transfer—at work in such events?

On the theory side, the mission of clarifying the SN engines is severely handicapped by the unavailability of multidimensional stellar evolution models that can reduce the major uncertainties of the stellar structure, rotation, and magnetic fields at the onset of core collapse. Clearly, reliable theoretical predictions of the progenitor-remnant connection and of explosion properties—energies, nucleosynthetic yields, asymmetries, remnant masses, and neutrino and GW signals—strongly depend on a thorough knowledge of the stellar conditions at the time the gravitational instability is reached.

DISCLOSURE STATEMENT

The author is not aware of any affiliations, memberships, funding, or financial holdings that might be perceived as affecting the objectivity of this review.

ACKNOWLEDGMENTS

LITERATURE CITED

1. Burbidge EM, Burbidge GR, Fowler WA, Hoyle F. *Rev. Mod. Phys.* 29:547 (1957)
2. Baade W, Zwicky F. *Phys. Rev.* 46:76 (1934)
3. Hoyle F, Fowler WA. *Astrophys. J.* 132:565 (1960)
4. Colgate SA, Johnson MH. *Phys. Rev. Lett.* 5:235 (1960)
5. Colgate SA, Grasberger WH, White RH. *Astron. J.* 66:280 (1961)
6. Colgate SA, White RH. *Astrophys. J.* 143:626 (1966)
7. Bethe HA, Wilson JR. *Astrophys. J.* 295:14 (1985)
8. Herant M, et al. *Astrophys. J.* 435:339 (1994)
9. Burrows A, Hayes J, Fryxell BA. *Astrophys. J.* 450:830 (1995)
10. Janka HT, Müller E. *Astrophys. J. Lett.* 448:109 (1995)
11. Janka HT, Müller E. *Astron. Astrophys.* 306:167 (1996)
12. Fryer CL, ed. *Astrophysics and Space Science Library*, vol. 302: *Stellar Collapse*. Dordrecht, Neth.: Kluwer Acad. (2004)
13. Mezzacappa A. *Annu. Rev. Nucl. Part. Sci.* 55:467 (2005)
14. Woosley SE, Janka HT. *Nat. Phys.* 1:147 (2005)
15. Woosley SE, Bloom JS. *Annu. Rev. Astron. Astrophys.* 44:507 (2006)
16. Kotake K, Sato K, Takahashi K. *Rep. Prog. Phys.* 69:971 (2006)
17. Janka HT, et al. *Phys. Rep.* 442:38 (2007)
18. Ott CD. *Class. Quantum Gravity* 26:063001 (2009)
19. Thielemann FK, Hirschi R, Liebendörfer M, Diehl R. *Lect. Notes Phys.* 812:153 (2011)
20. Wheeler JC. In *Supernovae: Jerusalem Winter School for Theoretical Physics*, ed. JC Wheeler, T Piran, S Weinberg, p. 1. Singapore: World Sci. (1990)
21. Nomoto K. *Astrophys. J.* 277:791 (1984)
22. Woosley SE, Heger A, Weaver TA. *Rev. Mod. Phys.* 74:1015 (2002)
23. Woosley SE, Weaver TA. *Astrophys. J. Suppl.* 101:181 (1995)
24. Tanaka M, et al. *Astrophys. J.* 692:1131 (2009)
25. Utrobin VP, Chugai NN. *Astron. Astrophys.* 532:A100 (2011)
26. Smartt SJ, Eldridge JJ, Crockett RM, Maund JR. *Mon. Not. R. Astron. Soc.* 395:1409 (2009)
27. Smartt SJ. *Annu. Rev. Astron. Astrophys.* 47:63 (2009)
28. Nomoto K. *Astrophys. J.* 322:206 (1987)
29. Poelarends AJT, Herwig F, Langer N, Heger A. *Astrophys. J.* 675:614 (2008)
30. Pumo ML, et al. *Astrophys. J. Lett.* 705:138 (2009)
31. Podsiadlowski P, et al. *Astrophys. J.* 612:1044 (2004)
32. Wanajo S, et al. *Astrophys. J.* 695:208 (2009)
33. Wanajo S, Janka HT, Müller B. *Astrophys. J. Lett.* 726:15 (2011)

34. Nomoto K, et al. *Nature* 299:803 (1982)
35. Hillebrandt W. *Astron. Astrophys.* 110:L3 (1982)
36. Heger A, Woosley SE, Spruit HC. *Astrophys. J.* 626:350 (2005)
37. Paczynski B. *Astrophys. J. Lett.* 494:45 (1998)
38. Iwamoto K, et al. *Nature* 395:672 (1998)
39. MacFadyen AI, Woosley SE. *Astrophys. J.* 524:262 (1999)
40. Popham R, Woosley SE, Fryer C. *Astrophys. J.* 518:356 (1999)
41. Fujimoto S, Nishimura N, Hashimoto M. *Astrophys. J.* 680:1350 (2008)
42. Yoon SC, Langer N. *Astron. Astrophys.* 443:643 (2005)
43. Woosley SE, Heger A. *Astrophys. J.* 637:914 (2006)
44. Heger A, et al. *Astrophys. J.* 591:288 (2003)
45. Woosley SE, Weaver TA. In *Proceedings of the Advanced Studies Institute*, ed. MJ Rees, RJ Stoneham, p. 79. Dordrecht, Neth.: D. Reidel Publ. (1982)
46. Fryer CL, Woosley SE, Heger A. *Astrophys. J.* 550:372 (2001)
47. Smith N, et al. *Astrophys. J.* 666:1116 (2007)
48. Gal-Yam A, et al. *Nature* 462:624 (2009)
49. Woosley SE, Blinnikov S, Heger A. *Nature* 450:390 (2007)
50. Kasen D, Bildsten L. *Astrophys. J.* 717:245 (2010)
51. Burrows A, Sawyer RF. *Phys. Rev. C* 58:554 (1998)
52. Horowitz CJ. *Phys. Rev. D* 65:043001 (2002)
53. Carter GW, Prakash M. *Phys. Lett. B* 525:249 (2002)
54. Reddy S, Prakash M, Lattimer JM, Pons JA. *Phys. Rev. C* 59:2888 (1999)
55. Langanke K, et al. *Phys. Rev. Lett.* 90:241102 (2003)
56. Horowitz CJ. *Phys. Rev. D* 55:4577 (1997)
57. Langanke K, et al. *Phys. Rev. Lett.* 100:011101 (2008)
58. Mezzacappa A, Bruenn SW. *Astrophys. J.* 405:669 (1993)
59. Bruenn SW. *Astrophys. J. Suppl.* 58:771 (1985)
60. Pons JA, Miralles JA, Ibanez JMA. *Astron. Astrophys. Suppl.* 129:343 (1998)
61. Hannestad S, Raffelt GG. *Astrophys. J.* 507:339 (1998)
62. Buras R, et al. *Astrophys. J.* 587:320 (2003)
63. Arnett WD. *Can. J. Phys.* 44:2553 (1966)
64. Wilson JR. *Astrophys. J.* 163:209 (1971)
65. LeBlanc JM, Wilson JR. *Astrophys. J.* 161:541 (1970)
66. Smarr L, Wilson JR, Barton RT, Bowers RL. *Astrophys. J.* 246:515 (1981)
67. Symbalisty EMD. *Astrophys. J.* 285:729 (1984)
68. Mönchmeyer R, Schäfer G, Müller E, Kates RE. *Astron. Astrophys.* 246:417 (1991)
69. Arnett WD, Bahcall JN, Kirshner RP, Woosley SE. *Annu. Rev. Astron. Astrophys.* 27:629 (1989)
70. Hillebrandt W, Höflich P. *Rep. Prog. Phys.* 52:1421 (1989)
71. Wilson JR, Mayle RW. *Phys. Rep.* 163:63 (1988)
72. Bruenn SW, Dineva T. *Astrophys. J. Lett.* 458:71 (1996)
73. Fryer CL, Warren MS. *Astrophys. J. Lett.* 574:65 (2002)
74. Fryer CL, Warren MS. *Astrophys. J.* 601:391 (2004)
75. Fryer CL, Young PA. *Astrophys. J.* 659:1438 (2007)
76. Scheck L, Janka HT, Foglizzo T, Kifonidis K. *Astron. Astrophys.* 477:931 (2008)
77. Sato J, Foglizzo T, Fromang S. *Astrophys. J.* 694:833 (2009)
78. Bruenn SW, De Nisco KR, Mezzacappa A. *Astrophys. J.* 560:326 (2001)
79. Lentz EJ, et al. *Astrophys. J.* 747:73 (2012)
80. Buras R, Rampp M, Janka HT, Kifonidis K. *Astron. Astrophys.* 447:1049 (2006)
81. Müller B, Janka HT, Marek A. arXiv:1202.0815 [astro-ph] (2012)
82. Blondin JM, Mezzacappa A. *Nature* 445:58 (2007)
83. Fernández R. *Astrophys. J.* 725:1563 (2010)
84. Blondin JM, Mezzacappa A, DeMarino C. *Astrophys. J.* 584:971 (2003)
85. Iwakami W, et al. *Astrophys. J.* 678:1207 (2008)

86. Iwakami W, et al. *Astrophys. J.* 700:232 (2009)
87. Nordhaus J, Burrows A, Almgren A, Bell J. *Astrophys. J.* 720:694 (2010)
88. Hanke F, Marek A, Müller B, Janka HT. arXiv:1108.4355 [astro-ph] (2011)
89. Ott CD, et al. *Phys. Rev. Lett.* 98:261101 (2007)
90. Ott CD, et al. *Phys. Rev. Lett.* 106:161103 (2011)
91. Rampp M, Janka HT. *Astron. Astrophys.* 396:361 (2002)
92. Marek A, et al. *Astron. Astrophys.* 445:273 (2006)
93. Scheidegger S, et al. *Astron. Astrophys.* 514:A51 (2010)
94. Scheck L, Kifonidis K, Janka HT, Müller E. *Astron. Astrophys.* 457:963 (2006)
95. Wongwathanarat A, Janka H, Müller E. *Astrophys. J. Lett.* 725:106 (2010)
96. Müller E, Janka HT, Wongwathanarat A. *Astron. Astrophys.* 537:A63 (2012)
97. Bruenn SW, et al. *J. Phys. Conf. Ser.* 180:012018 (2009)
98. Takiwaki T, Kotake K, Suwa Y. *Astron. Astrophys.* 749:98 (2012)
99. Liebendörfer M, et al. *Prog. Theor. Phys. Suppl.* 186:87 (2010)
100. Yamada S, Janka HT, Suzuki H. *Astron. Astrophys.* 344:533 (1999)
101. Liebendörfer M, et al. *Astrophys. J. Suppl.* 150:263 (2004)
102. Burrows A, et al. *Astrophys. J.* 539:865 (2000)
103. Müller B, Janka HT, Dimmelmeier H. *Astrophys. J. Suppl.* 189:104 (2010)
104. Buras R, Janka HT, Rampp M, Kifonidis K. *Astron. Astrophys.* 457:281 (2006)
105. Kitaura FS, Janka HT, Hillebrandt W. *Astron. Astrophys.* 450:345 (2006)
106. Marek A, Janka HT. *Astrophys. J.* 694:664 (2009)
107. Hüdepohl L, et al. *Phys. Rev. Lett.* 104:251101 (2010)
108. Burrows A, et al. *Astrophys. J.* 640:878 (2006)
109. Burrows A, et al. *Astrophys. J.* 655:416 (2007)
110. Burrows A, et al. *Astrophys. J.* 664:416 (2007)
111. Ott CD, Burrows A, Dessart L, Livne E. *Astrophys. J.* 685:1069 (2008)
112. Brandt TD, Burrows A, Ott CD, Livne E. *Astrophys. J.* 728:8 (2011)
113. Swesty FD, Myra ES. *Astrophys. J. Suppl.* 181:1 (2009)
114. Obergaulinger M, Janka HT. arXiv:1101.1198 [astro-ph] (2011)
115. Liebendörfer M, Whitehouse SC, Fischer T. *Astrophys. J.* 698:1174 (2009)
116. Suwa Y, et al. *Publ. Astron. Soc. Jpn.* 62:L49 (2010)
117. Sumiyoshi K, Yamada S. *Astrophys. J. Suppl.* 199:17 (2012)
118. Bonazzola S, Vasset N. arXiv:1104.5330 [physics.comp-ph] (2011)
119. Shibata M, et al. *Prog. Theor. Phys.* 125:1255 (2011)
120. Liebendörfer M, Rampp M, Janka HT, Mezzacappa A. *Astrophys. J.* 620:840 (2005)
121. Hillebrandt W, Nomoto K, Wolff RG. *Astron. Astrophys.* 133:175 (1984)
122. Hebeler K, Lattimer JM, Pethick CJ, Schwenk A. *Phys. Rev. Lett.* 105:161102 (2010)
123. Demorest PB, et al. *Nature* 467:1081 (2010)
124. Lattimer JM, Prakash M. arXiv:1012.3208 [astro-ph] (2010)
125. Steiner AW, Lattimer JM, Brown EF. *Astrophys. J.* 722:33 (2010)
126. Lattimer JM, Swesty FD. *Nucl. Phys. A* 535:331 (1991)
127. Shen H, Toki H, Oyamatsu K, Sumiyoshi K. *Nucl. Phys. A* 637:435 (1998)
128. Lattimer JM, Pethick CJ, Ravenhall DG, Lamb DQ. *Nucl. Phys. A* 432:646 (1985)
129. Janka HT, et al. *Nucl. Phys. A* 758:19 (2005)
130. Lentz E, et al. arXiv:1101.0156 [astro-ph] (2010)
131. Hempel M, Fischer T, Schaffner-Bielich J, Liebendörfer M. *Astrophys. J.* 748:70 (2012)
132. Lattimer JM, Prakash M. *Phys. Rep.* 333:121 (2000)
133. Shlomo S, Kolomietz VM, Colò G. *Eur. Phys. J. A* 30:23 (2006)
134. Piekarewicz J. *J. Phys. G* 37:064038 (2010)
135. Swesty FD, Lattimer JM, Myra ES. *Astrophys. J.* 425:195 (1994)
136. Thompson TA, Burrows A, Pinto PA. *Astrophys. J.* 592:434 (2003)
137. Roberts LF, et al. *Phys. Rev. Lett.* 108:061103 (2012)
138. Hempel M, Schaffner-Bielich J. *Nucl. Phys. A* 837:210 (2010)

139. Shen G, Horowitz CJ, Teige S. *Phys. Rev. C* 83:035802 (2011)
140. Shen G, Horowitz CJ, O'Connor E. *Phys. Rev. C* 83:065808 (2011)
141. Shen H, Toki H, Oyamatsu K, Sumiyoshi K. *Astrophys. J. Suppl.* 197:20 (2011)
142. Sumiyoshi K, Röpke G. *Phys. Rev. C* 77:055804 (2008)
143. Typel S, et al. *Phys. Rev. C* 81:015803 (2010)
144. Hempel M, Schaffner-Bielich J, Typel S, Röpke G. *Phys. Rev. C* 84:055804 (2011)
145. Arcones A, et al. *Phys. Rev. C* 78:015806 (2008)
146. Müller B, et al. arXiv:1112.1913 [astro-ph] (2011)
147. Gershtein SS, et al. *J. Exp. Theor. Phys.* 69:1473 (1976)
148. Chechetkin VM, et al. *Phys. Lett. B* 62:100 (1976)
149. Zmitrenko NV, Imshennik VS, Khlopov MI, Chechetkin VM. *J. Exp. Theor. Phys.* 75:1169 (1978)
150. Chechetkin VM, et al. *Astrophys. Space Sci.* 67:61 (1980)
151. Bethe HA. *Rev. Mod. Phys.* 62:801 (1990)
152. Mazurek TJ. *Astrophys. J. Lett.* 259:13 (1982)
153. Hix WR, et al. *Phys. Rev. Lett.* 91:201102 (2003)
154. Janka HT. *Astron. Astrophys.* 368:527 (2001)
155. Foglizzo T, Scheck L, Janka HT. *Astrophys. J.* 652:1436 (2006)
156. Janka HT, Kifonidis K, Rampp M. *Lect. Notes Phys.* 578:333 (2001)
157. Janka HT, Keil W. arXiv:astro-ph/9709012 (1997)
158. Janka HT, Müller B, Kitaura FS, Buras R. *Astron. Astrophys.* 485:199 (2008)
159. Fischer T, et al. *Astron. Astrophys.* 517:A80 (2010)
160. Müller B, Janka HT, Heger A. arXiv:1205.7078 [astro-ph] (2012)
161. Ott CD, O'Connor EP, Dasgupta B. arXiv:1111.6282 [astro-ph] (2011)
162. Chakraborty S, et al. *Phys. Rev. Lett.* 107:151101 (2011)
163. Chakraborty S, et al. *Phys. Rev. D* 84:025002 (2011)
164. Dasgupta B, O'Connor EP, Ott CD. *Phys. Rev. D* 85:065008 (2012)
165. Sarikas S, Raffelt GG, Hüdepohl L, Janka HT. *Phys. Rev. Lett.* 108:061101 (2012)
166. Murphy JW, Burrows A. *Astrophys. J.* 688:1159 (2008)
167. Blondin JM, Mezzacappa A. *Astrophys. J.* 642:401 (2006)
168. Ohnishi N, Kotake K, Yamada S. *Astrophys. J.* 641:1018 (2006)
169. Foglizzo T, Galletti P, Scheck L, Janka HT. *Astrophys. J.* 654:1006 (2007)
170. Guilet J, Foglizzo T. *Mon. Not. R. Astron. Soc.* 421:546 (2012)
171. Foglizzo T, Masset F, Guilet J, Durand G. *Phys. Rev. Lett.* 108:051103 (2012)
172. Foglizzo T. *Astron. Astrophys.* 368:311 (2001)
173. Foglizzo T. *Astron. Astrophys.* 392:353 (2002)
174. Burrows A, Goshy J. *Astrophys. J. Lett.* 416:75 (1993)
175. Yamasaki T, Yamada S. *Astrophys. J.* 623:1000 (2005)
176. Yamasaki T, Yamada S. *Astrophys. J.* 650:291 (2006)
177. Pejcha O, Thompson TA. *Astrophys. J.* 756:106 (2012)
177a. Keshet U, Balberg S. *Phys. Rev. Lett.* 108:251101 (2012)
178. Fernández R. *Astrophys. J.* 749:142 (2012)
179. Thompson TA, Quataert E, Burrows A. *Astrophys. J.* 620:861 (2005)
180. Murphy JW, Meakin C. *Astrophys. J.* 742:74 (2011)
181. Yamasaki T, Yamada S. *Astrophys. J.* 656:1019 (2007)
182. Fernández R, Thompson C. *Astrophys. J.* 703:1464 (2009)
183. Yamasaki T, Foglizzo T. *Astrophys. J.* 679:607 (2008)
184. Burrows A, Dolence JC, Murphy JW. arXiv:1204.3088 [astro-ph] (2012)
185. Murphy JW, Dolence JC, Burrows A. arXiv:1205.3491 [astro-ph] (2012)
186. Bisnovatyi-Kogan GS. *Astron. J.* 47:813 (1970)
187. Ostriker JP, Gunn JE. *Astrophys. J. Lett.* 164:95 (1971)
188. Meier DL, Epstein RI, Arnett WD, Schramm DN. *Astrophys. J.* 204:869 (1976)
189. Bisnovatyi-Kogan GS, Popov IP, Samokhin AA. *Astrophys. Space Sci.* 41:287 (1976)
190. Kotake K, Sawai H, Yamada S, Sato K. *Astrophys. J.* 608:391 (2004)

191. Sawai H, Kotake K, Yamada S. *Astrophys. J.* 631:446 (2005)
192. Obergaulinger M, Aloy MA, Dimmelmeier H, Müller E. *Astron. Astrophys.* 457:209 (2006)
193. Moiseenko SG, Bisnovatyi-Kogan GS, Ardeljan NV. *Mon. Not. R. Astron. Soc.* 370:501 (2006)
194. Balbus SA, Hawley JF. *Rev. Mod. Phys.* 70:1 (1998)
195. Akiyama S, Wheeler JC, Meier DL, Lichtenstadt I. *Astrophys. J.* 584:954 (2003)
196. Obergaulinger M, Cerdá-Durán P, Müller E, Aloy MA. *Astron. Astrophys.* 498:241 (2009)
197. Wheeler JC, Meier DL, Wilson JR. *Astrophys. J.* 568:807 (2002)
198. Charpinet S, Fontaine G, Brassard P. *Nature* 461:501 (2009)
199. Meynet G, Eggenberger P, Maeder A. *Astron. Astrophys.* 525:L11 (2011)
200. Thompson C, Duncan RC. *Astrophys. J.* 408:194 (1993)
201. Endeve E, Cardall CY, Budiardja RD, Mezzacappa A. *Astrophys. J.* 713:1219 (2010)
202. Guilet J, Foglizzo T, Fromang S. *Astrophys. J.* 729:71 (2011)
203. Suzuki TK, Sumiyoshi K, Yamada S. *Astrophys. J.* 678:1200 (2008)
204. Burrows A, Dessart L, Ott CD, Livne E. *Phys. Rep.* 442:23 (2007)
205. Weinberg NN, Quataert E. *Mon. Not. R. Astron. Soc.* 387:L64 (2008)
206. Sagert I, et al. *Phys. Rev. Lett.* 102:081101(2009)
207. Fischer T, et al. *Astrophys. J. Suppl.* 194:39 (2011)
208. Prakash M, Cooke JR, Lattimer JM. *Phys. Rev. D* 52:661 (1995)
209. Fischer T, et al. *Phys. At. Nucl.* 75:613 (2012)
210. Dasgupta B, et al. *Phys. Rev. D* 81:103005 (2010)
211. Sumiyoshi K, Yamada S, Suzuki H. *Astrophys. J.* 688:1176 (2008)
212. Fischer T, et al. *Astron. Astrophys.* 499:1 (2009)
213. Marek A, Janka HT, Müller E. *Astron. Astrophys.* 496:475 (2009)
214. Lund T, et al. *Phys. Rev. D* 82:063007 (2010)
215. Fischer T, Martínez-Pinedo G, Hempel M, Liebendörfer M. *Phys. Rev. D* 85:083003 (2012)
216. Roberts LF. arXiv:1205.3228 [astro-ph] (2012)
217. Roberts LF, Reddy S. arXiv:1205.4066 [astro-ph] (2012)
218. Martínez-Pinedo G, Fischer T, Lohs A, Huther L. arXiv:1205.2793 [astro-ph] (2012)
219. Thompson TA, Burrows A, Horvath JE. *Phys. Rev. C* 62:035802 (2000)
220. Keil MT, Raffelt GG, Janka HT. *Astrophys. J.* 590:971 (2003)
221. Raffelt GG. *Astrophys. J.* 561:890 (2001)
222. Tubbs DL. *Astrophys. J.* 231:846 (1979)
223. Serpico PD, et al. *Phys. Rev. D* 85:085031 (2012)
224. Banerjee P, Haxton WC, Qian YZ. *Phys. Rev. Lett.* 106:201104 (2011)
225. Duan H, Friedland A, McLaughlin GC, Surman R. *J. Phys. G* 38:035201 (2011)
226. Murphy JW, Ott CD, Burrows A. *Astrophys. J.* 707:1173 (2009)
227. Ott CD, Burrows A, Dessart L, Livne E. *Phys. Rev. Lett.* 96:201102 (2006)
228. Kotake K, Iwakami W, Ohnishi N, Yamada S. *Astrophys. J. Lett.* 697:133 (2009)
229. Kotake K. arXiv:1110.5107 [astro-ph] (2011)
230. Qian YZ, Woosley SE. *Astrophys. J.* 471:331 (1996)
231. Thompson TA, Burrows A, Meyer BS. *Astrophys. J.* 562:887 (2001)
232. Hoffman RD, Woosley SE, Qian YZ. *Astrophys. J.* 482:951 (1997)
233. Takahashi K, Witti J, Janka HT. *Astron. Astrophys.* 286:857 (1994)
234. Roberts LF, Woosley SE, Hoffman RD. *Astrophys. J.* 722:954 (2010)
235. Fröhlich C, et al. *Phys. Rev. Lett.* 96:142502 (2006)
236. Pruet J, et al. *Astrophys. J.* 644:1028 (2006)
237. Tamborra I, Raffelt GG, Hüdepohl L, Janka HT. *J. Cosmol. Astropart. Phys.* 1:13 (2012)
238. Hammer NJ, Janka HT, Müller E. *Astrophys. J.* 714:1371 (2010)
239. Ugliano M, Janka HT, Marek A, Arcones A. arXiv:1205.3657 [astro-ph] (2012)
240. Hobbs G, Lorimer DR, Lyne AG, Kramer M. *Mon. Not. R. Astron. Soc.* 360:974 (2005)
241. Lai D, Chernoff DF, Cordes JM. *Astrophys. J.* 549:1111 (2001)
242. Janka HT, Müller E. *Astron. Astrophys.* 290:496 (1994)
243. Burrows A, Hayes J. *Phys. Rev. Lett.* 76:352 (1996)

244. Arnett WD, Meakin C. *Astrophys. J.* 733:78 (2011)
245. Kusenko A, Mandal BP, Mukherjee A. *Phys. Rev. D* 77:123009 (2008)
246. Scheck L, et al. *Phys. Rev. Lett.* 92:011103 (2004)
247. Nordhaus J, et al. *Phys. Rev. D* 82:103016 (2010)
248. Nordhaus J, Brandt T, Burrows A, Almgren A. *Mon. Not. R. Astron. Soc.* 423:1805 (2012)
249. Rantsiou E, Burrows A, Nordhaus J, Almgren A. *Astrophys. J.* 732:57 (2011)
250. Ott CD, et al. *Astrophys. J. Suppl.* 164:130 (2006)
251. Kifonidis K, Plewa T, Janka HT, Müller E. *Astron. Astrophys.* 408:621 (2003)
252. Kifonidis K, et al. *Astron. Astrophys.* 453:661 (2006)
253. Casares J. *Int. Astron. Union Symp.* 238:3 (2007)
254. Ziolkowski J. *Mem. Soc. Astron. It.* 81:294 (2010)
255. Belczynski K, et al. arXiv:1110.1635 [astro-ph] (2011)
256. Fryer CL, et al. *Astrophys. J.* 749:91 (2012)
257. Zhang W, Woosley SE, Heger A. *Astrophys. J.* 679:639 (2008)
258. O'Connor E, Ott CD. *Astrophys. J.* 730:70 (2011)
259. Pejcha O, Thompson TA, Kochanek CS. *Mon. Not. R. Astron. Soc.* 424:1570 (2012)
260. Kachelrieß M, et al. *Phys. Rev. D* 71:063003 (2005)
261. Ellis J, et al. *Phys. Rev. D* 085:045032 (2012)
262. Ellis J, et al. *Phys. Rev. D* 85:105028 (2012)

Contents

Indexes

Errata

An online log of corrections to *Annual Review of Nuclear and Particle Science* articles may
be found at http://nucl.annualreviews.org/errata.shtml